

LMNA R527C mutation causes an inflammation driven progeria via triggering DNA-sensing pathways

Yingchi Zhao

Institute of Systems Biomedicine <https://orcid.org/0000-0002-8698-6864>

Wei Shu

Guangxi Medical University

Xiaoyu Liu

Shandong University

Xuyao Jiao

Shandong University <https://orcid.org/0000-0002-9110-2234>

Jianshuang Li

The First Affiliated Hospital, Jinan University

Tao Liu

Shenzhen Luohu People's Hospital, the 3rd Affiliated Hospital of Shenzhen University

Ming Kuang

Peking University Health Science Center

Ridong Li

Peking University Health Science Center

Hongqiang Du

Peking University

Zeming Zhang

Institute of Systems Biomedicine, Department of Immunology, School of Basic Medical Sciences, Beijing Key Laboratory of Tumor Systems Biology, Peking University Health Science Center, Beijing, China

<https://orcid.org/0000-0002-0307-5716>

Zhe Zhou

Peking University Health Science Center

Xuefei Guo

Peking University Health Science Center

Xuemei Wei

Institute of Systems Biomedicine, Department of Immunology, School of Basic Medical Sciences, Beijing Key Laboratory of Tumor Systems Biology, Peking University Health Science Center, Beijing, China

Dandan Wang

peking university

Tongtong Liu

Peking University Health Science Center

Yunfei Li

Institute of Systems Biomedicine, Department of Immunology, School of Basic Medical Sciences, Beijing Key Laboratory of Tumor Systems Biology, Peking University Health Science Center, Beijing, China

Shengde Liu

Peking University Health Science Center

Jingxuan Chen

Peking University Health Science Center

Yujie Luo

Institute of Systems Biomedicine, Department of Immunology, School of Basic Medical Sciences, Beijing Key Laboratory of Tumor Systems Biology, Peking University Health Science Center, Beijing, China

Huawei Xia

Peking University Health Science Center

Lili Cao

Peking University Health Science Center

Wenmin Tian

Center for Precision Medicine Multi-Omics Research, Peking University Health Science Center, Peking University

Xue Sun

Peking University Health Science Center

Wei Dong

Institute of Laboratory Animal Science, Chinese Academy of Medical Sciences and Peking Union Medical College

Guangqian Zhou

Shenzhen University

Xiang Gao

Shandong University <https://orcid.org/0000-0001-6397-5639>

Qinghua Zhou

The First Affiliated Hospital, Jinan University

Fuping You (✉ fupingyou@hsc.pku.edu.cn)

School of Basic Medical Sciences, Beijing Key Laboratory of Tumor Systems Biology, Peking University Health Science Center

Article**Keywords:****Posted Date:** March 10th, 2022

DOI: <https://doi.org/10.21203/rs.3.rs-1406652/v1>

License:  This work is licensed under a Creative Commons Attribution 4.0 International License.

[Read Full License](#)

Abstract

Homozygous mutations in Ig-like domain of LMNA cause severe progeria. Unlike typical HGPS mediated by progerin due to LMNAWT/G608G mutation, it remains elusive how these homozygous mutations cause progeria. We here found that patients with LMNAR527C/R527C mutation developed an atypical progeria with autoimmune symptoms. Compare to LMNAWT/G608G mutation, this mutation led to more severe inflammation in patients. MSCs from LMNAR527C/R527C patients exhibited overt inflammation and cellular senescence. Mechanistically, LMNAR527C/R527C mutation attenuated its binding to DNA binding protein BAF, which led to aberrant aggregation of Lamin A and activation of DNA sensing pathways. Inhibition of DNA sensors, cGAS or AIM2, can suppress inflammation and rescue the senescence of patient-derived MSCs. LmnaR527C/R527C mice showed enhanced inflammation, and developed accelerated aging and dead at an early age after high-fat diet (HFD) feeding, which could be rescued by deficiency of AIM2 or treatment by a small molecule inhibitor of cGAS-STING. Therefore, we demonstrated that LMNAR527C/R527C mutation damped its interaction with DNA-binding proteins and exposed damaged DNA to the cytosolic DNA sensors, which triggered aberrant inflammatory responses and promoted the onset of accelerated aging. The present study uncovered that an inflammation driven progeria was caused by LMNA mutation and DNA sensing pathways could be potential therapeutic targets for progeria syndromes caused by homozygous mutations in Ig-like domain of LMNA.

Introduction

Lamin proteins are components of the nuclear lamina and belong to the type V intermediate filament family¹. There are three types of lamins in human cells: A, B, and C. Lamin A and Lamin C are coded by *LMNA*. Lamin B1 and Lamin B2 are coded by *LMNB1* and *LMNB2* respectively². Similar to other filament proteins, a Lamin protein contains a N-terminal Head domain, a α -helical rod domain in the middle and a C-terminal immunoglobulin like tail domain. The rod domain mediates homodimer formation of Lamin proteins. Moreover, with help of other proteins, Head domain and Tail domain mediate formation of Intermediate filaments, and further assembly of nuclear lamina, a fibrous layer on the nucleoplasmic side of the inner nuclear membrane³⁻⁵. Accumulating studies showed that nuclear lamina played an important role in nuclear assembly, chromatin organization, nuclear membrane stability, DNA replication, DNA damage repair, gene transcription and telomere dynamics⁶⁻¹⁰. The expression of *LMNA* is very high in terminally differentiated epidermal cells, whereas extremely low in stem cells. B-type Lamins are widely expressed at relative high level in different tissues and cells except hepatocytes^{11,12}. For subcellular distribution, B-type Lamins are exclusively localized on nuclear lamina. In addition to nuclear lamina, A-type Lamin is also distributed in nuclear matrix indicating Lamin A is a multi-functional protein in nucleus^{13,14}.

Naturally occurring mutations in *LMNA* have been shown to be responsible for distinct diseases called laminopathies. The Universal Mutation Database (UMD) has included more than 500 mutations of *LMNA* that resulted in laminopathies involving different tissues and organs, such as, neuromuscular

abnormalities: Dilated Cardiomyopathy (DCM)¹⁵, Emery-Dreifuss muscular dystrophy (EDMD)¹⁶, limb girdle muscular dystrophy type 1B (LGMD1B)¹⁷; Metabolic diseases: familial partial Lipodystrophy (FPLD)¹⁸; Progeria syndrome: Hutchinson-Gilford progeria (HGPS)^{19,20}, Mandibuloacral dysplasia (MAD)²¹, Restrictive dermopathy (RD)²², atypical Werner's syndrome (WRN)²³. Despite intensive effort have been devoted to clarify the mechanism of laminopathies, it remains elusive how different mutants of *LMNA* result in dysfunction of different organs and biological processes. In addition to *LMNA*, mutations of Lamin A interacting proteins also cause similar diseases²⁴. For example, mutation of *EMD*, *LAP2*, *BANF1* or *ZMPSTE24* causes Emery-Dreifuss muscular dystrophy (EDMD), Dilated Cardiomyopathy (DCM), Nestor-Guillermo Progeria Syndrome (NGPS) or RD and MAD respectively^{7,25-29}. Complex cellular and molecular mechanisms are involved in the pathogenesis of these laminopathies, which make it very difficult to gain further insight and find out the therapeutic targets of these diseases²⁴. However, all those mutations are *LMNA* or Lamin A binding proteins related, which strengthens the point that Lamin A plays a pivotal role in these diseases and also suggests that Lamin A interacts with different signaling pathways³⁰.

The identification of progeria syndrome is relatively later than other laminopathies¹⁹⁻²¹. However, after its emergency, progeria seated in the forefront of scientific efforts. HGPS is most intensively investigated progeria syndrome and resulted from a heterozygous mutation of *LMNA* at G608G (c.1824 C > T). This mutation caused aberrant splicing of mRNA and generated a new truncated Lamin A. This mutant Lamin A, called progerin, was not able to interact with zinc metallopeptidase STE24 (ZMPST24) that mediated farnesylation of Lamin A³¹. Progerin showed cytotoxicity by disrupting the function of wild type Lamin A. Moreover, two other heterozygous mutations also cause aberrant splicing and increased expression of progerin³². However, a panel of mutations of *LMNA* also caused progeria syndrome without leading to alternative splicing^{33,34}, including R435C, V440M, R471C, R527C, R527L, R527H, A529T, M540I, K542N, S573L and G592R³⁵⁻⁴³. Different from HGPS, these diseases were caused by homozygous mutation of *LMNA* at according sites. Moreover, those patients showed more severe autoimmune symptom than HGPS, such as arthritis or scleroderma like features^{39,43,44}. These clinical data suggested dysfunction of immune system or dysregulation of inflammatory responses in these atypical progeria syndromes. Interestingly, the according amino acid residues of all these homozygous mutations were exposed on the surface of Ig-like fold domain and clustered in distinct regions that overlap a predicted binding pocket⁴⁵. This indicated these mutations might cause development of premature aging via a similar mechanism, however, which has not been elucidated.

It has been reported that DNA sensing pathways played important roles in cell senescence^{46,47}. CGAS (Cyclic GMP-AMP synthase) recognized naked DNA and activated transcription of Type I interferons (IFNs) and interferon stimulated genes (ISGs)^{48,49}. Another DNA sensor AIM2 (Absent in melanoma 2) activated secretion of proinflammatory cytokines^{50,51}. Deficiency of either of these sensors was able to rescue senescence of cells^{48,50}. In addition to *LMNA* and *LMNA* related genes, mutation of genes involved in DNA replication and DNA damage repair also resulted in premature aging, such as WRN, ATM

and ERCC^{28,52}. Thus, accumulation of damaged DNA and DNA sensing pathways could promote inflammation, which probably contributed the pathogenesis of progeria syndromes. Progerin disrupted cell cycle and DNA replication by downregulating *LAP2* and Lamin A-LAP2 α -RB signaling^{53–55}, which could activate inflammatory responses⁵⁶. However, the mutations within C-terminus of Lamin A caused severe inflammation than G608G mutation⁵⁷. It remains unknown how these mutations activate inflammatory responses.

We here found that children from three different Chinese families carried homozygous *LMNA* mutation at R527C (c.1579C > T), which caused an atypical progeria syndrome. These patients exhibited apparent autoimmune symptoms. The MSCs from patients, macrophages and MEFs from *Lmna*^{R527C/R527C} mice developed cellular senescence and enhanced inflammatory responses. *Lmna*^{R527C/R527C} mice showed enhanced inflammation spontaneously. Interestingly, HFD feeding induced progeria syndrome in mutant but not wild type mice, which led to early death and telomere shortening of mutant mice. Deficiency or inhibition of cGAS-STING or AIM2 pathways suppressed inflammation and rescued the death of mice from accelerated aging. Thus, inflammation is the cause and driven force of this atypical progeria. Mechanistically, R527C mutation of *LMNA* damped its interaction with DNA binding proteins, including BAF, which cause aberrant aggregation of Lamin A, dysfunction of lamina-associated domains (LADs) and DNA sensing. Consequently, gene transcription was downregulated globally, including the genes controlling cell proliferation and survival. Moreover, damaged and naked DNA was accumulated, which activated DNA sensing pathways and inflammatory responses.

Results

LMNA mutant R527C results in an atypical Hutchinson-Gilford progeria syndrome with overt inflammation

We found six children, from three different Chinese families, were HGPS-like patients and carried *LMNA* mutation (c.1579C > T, p.R527C). These three families implied that this syndrome may possess autosomal recessive inheritance characteristic (Fig. 1a,b and Extended Data Fig. 1a,b). While the classical G608G HGPS is autosomal dominant. All the patients had the typical appearances of progeria syndrome along with elevated level of blood platelet and decreased level of blood creatinine. qRT-PCR analysis showed that their telomeres were significantly shorter than according siblings (Fig. 1c). These children showed more severe scleroderma-like change and acroosteolysis symptoms (Fig. 1d,e). Both Scleroderma and acroosteolysis are believed to be autoimmune associated diseases^{58,59}, which promoted us to explore the role of immune responses in pathogenesis of this atypical progeria. We isolated the RNA of PBMCs from patients and healthy donors, and performed whole genome wide RNA-seq analysis (Fig. 1f). Consistent with the premature phenotypes of patients, the down-regulated genes were enriched in cell proliferation and DNA replication (Fig. 1g). Interestingly, up-regulated genes were predominantly enriched in the pathways of immune responses, including antigen processing and presentation, interferon-gamma-mediated signaling pathway, type I interferon signaling pathway and

defense response to virus (Fig. 1h and Extended Data Fig. 1c). Type I interferon was believed to be the primary effector that mediated the elimination of invading virus. We further examined the expression of related genes in patients and healthy donors. A panel of interferon stimulated genes (ISGs) were significantly increased in patients (Fig. 1i and Extended Data Fig. 1d), indicating an antiviral like response was activated. In line with this, the pattern recognition receptors (PRRs) responsible for sensing foreign pathogens or endogenous danger signals were also upregulated in patients (Fig. 1j).

To gain further insight of the cellular mechanism of this disease, we reprogrammed the PBMCs of patients and healthy donors into iPSCs (induced pluripotent stem cells) (Fig. 1f). Consistent with the reported result¹², the expression of Lamin A was extremely low in iPSCs. Thus, the viability of patient-derived iPSCs and control iPSCs was comparable. To this end, we induced these iPSCs to be differentiated into Mesenchymal stem cells (MSC). Lamin A was highly expressed in these MSCs (Extended Data Fig. 1e). Patient-derived MSCs exhibited lower cell viability and higher β -galactosidase activity than control MSCs (Extended Data Fig. 1f,g), suggesting that patient-derived MSCs underwent cellular senescence. To elucidate the mechanism by which Lamin A R527C mutation caused senescence, we performed whole genome wide RNA-seq of patient-derived MSCs and control MSCs (Fig. 1f), and compared the differentially expressed genes between $LMNA^{R527C/R527C}$ and $LMNA^{WT/G608G}$ (GEO ID 200175733). Consistent with the result from patient blood RNA-seq, down-regulated genes of both mutations were enriched in DNA replication and cellular development (Fig. 1k). Interestingly, the up-regulated genes in $LMNA^{R527C/R527C}$ patient-derived MSC were enriched in innate immunity and inflammation. However, these immune related genes were not upregulated in cells from $LMNA^{WT/G608G}$ patients (Fig. 1l and Extended Data Fig. 1h-j). Together, compared to $LMNA^{WT/G608G}$, the atypical progeria with $LMNA$ R527C mutation caused more significant inflammatory responses.

Lamin A R527C mutation damped its interaction with DNA binding proteins

To clarify the mechanism by which Lamin A R527C mutation caused cell senescence, we purified wild type and mutant Lamin A protein and examined their property and function *in vitro*. Similar protein aggregation was observed between wild type and mutant Lamin A (Fig. 2a). Moreover, wild type and mutant Lamin A exhibited similar capability to form droplet and filament *in vitro* (Extended Data Fig. 2a). This was supported by a reported study that showed Arginine 527C mutation did affect its stability and ability to form filament³³. It is notable that $LMNA$ G608G is a gain-of-function mutation³¹, but R527C is a loss-of-function mutation (Fig. 1b and Extended Data Fig. 1a). As mentioned above, this homozygous mutation did not affect its own property and function. We reasoned that this mutation might damp its interaction with other proteins. Therefore, we performed co-immunoprecipitation and mass spectrometry with MSCs derived from patients and healthy controls (Fig. 2b). 400 proteins were identified to interact with wild type Lamin A, among which 44 proteins were previously reported Lamin A interacting partners (Fig. 2c). We then analyzed the differentially interacting proteins with wild type and mutant Lamin A. 54.17% of these proteins showed similar affinity with mutant Lamin A compared with wild type Lamin A.

37.5% of the known Lamin A associated proteins were not able to interact with mutant Lamin A, or showed significant decreased interaction (Fig. 2c). This result was in line with the fact that R527C mutation is a loss-of-function mutation. GO analysis showed that those protein were predominantly enriched in DNA binding process (Fig. 2d,e), suggesting that Lamin A R527C mutation damped its interaction with DNA binding associated complex. Among them, BAF is a well-known Lamin A associated protein with extremely high DNA binding affinity (Fig. 2f). Co-crystallization assay showed that the 527 Arginine of Lamin A and 12 Alanine of BAF were critical for the direct interaction between these two proteins⁶⁰. Interestingly, a single amino acid substitution of BAF in humans (Ala12Thr) causes Nestor-Guillermo progeria syndrome (NGPS), another kind of progeria²⁷. The mass spectrometry detected BAF after immunoprecipitation with wild type but not R527C mutant Lamin A. Co-immunoprecipitation assay confirmed that the interaction between Lamin A and BAF was greatly attenuated after 527 Arginine substitution (Fig. 2g). Consistently, a previous study demonstrated that Lamin A R527H mutation blocked its interaction with BAF⁶⁰. Accordingly, Lamin A was not able to interact with BAF with A12T mutation (Fig. 2i). However, G608G or other pathological mutations of Arginine did not affect its interaction with BAF (Fig. 2h). It is believed that homodimers of BAF can bind simultaneously to DNA, lamins, and INM proteins harboring a LEM (LAP2, Emerin, MAN1) domain, thus serving as a bridging factor⁶¹. We also examined the interaction between Lamin A and LAP2 α , another important interacting partner of Lamin A with DNA binding property. Consistent with the mass spectrometry data, R527C mutation but not G608G mutation damped its interaction with LAP2 α (Extended Data Fig. 2b,c). Together, R527C mutation of Lamin A significantly damaged its protein interactome, particularly the proteins with DNA binding property. Same to R527C mutation, all disease related homozygous mutations were exposed on the surface of Ig-like fold domain and clustered in distinct regions that overlap a predicted binding pocket. We further evaluated the interaction of these mutant proteins with BAF and LAP2 α . Most of these mutations damped the interaction between Lamin A and LAP2 α . Some of these mutants were unable to interact with BAF (Fig. 2j and Extended Data Fig. 2d). These results suggested that Ig-like fold domain of Lamin A was critical for its binding to DNA complex proteins, which may govern the pathogenesis of different kinds of laminopathy diseases.

R527C mutation promotes self-aggregation of Lamin A

Most Lamin A locates next to the inner nuclear membrane. Proper localization is required for its physiological function. We then examined the cellular localization of Lamin A with confocal microscopy in control and patient-derived MSCs. Wild type Lamin A predominantly localized on the nuclear lamina. Interestingly, the R527C Lamin A formed foci on the nuclear lamina and in the nucleus (Fig. 3a). Consistently, the reconstituted R527C mutant but not wild type GFP-Lamin A formed foci in Lamin A knockout cells (Fig. 3b and Extended Data Fig. 3a-c). Moreover, fluorescence was recovered within 2 minutes after photobleaching (FLIP, fluorescence loss in photobleaching) indicating that phase separation might occur during overexpression of R527C GFP-Lamin A (Extended Data Fig. 3d). Lamin A is a member of the intermediate filament (IF) family proteins, which constitute a major component of the nucleoskeleton⁶². Lamin A is composed of three units that are common among intermediate filaments: a

central α -helical rod domain containing heptad repeats surrounded by globular N and C-terminal domains. The N-terminal is shorter and located at the top (head) while the C-terminal is longer and located at the end (tail)³⁻⁵ (Fig. 3c). The head domain of lamins is fairly consistent, the composition of the tail domain varies based on the type of lamins. Similar to other IF proteins, lamins self-assemble into more complex structures. The basic unit of these structures is a coiled-coil dimer. The dimers arrange themselves in a head-to-tail manner, allowing for the formation of a protofilament. As these protofilaments aggregate, they form lamin filaments with the help of relevant proteins, such as BAF and LAP2 α . To investigate if R527C mutation affects the construct and filament formation of Lamin A, we examined the subcellular localization with confocal microscopy (Fig. 3d). The N-terminal truncation (1-390) without NLS (nuclear localization sequence) formed big foci in cytoplasm. The N-terminal protein with NLS formed foci in nucleus. The C-terminal proteins dispersed in cytoplasm or nucleus when NLS was deleted or not (Fig. 3d and Extended Data Fig. 3e,f). This data suggested that the rod domain mediated the foci formation. On the other hand, the C-terminal domain disrupted foci formation in the cell. As R527C mutant Lamin A formed foci and was not able to bind to BAF and LAP2 α effectively. We guessed that aggregation of Lamin A disturbed its interaction with BAF and LAP2 α , or on the other hand, loss of interaction with these proteins resulted in aggregation of mutant Lamin A. To this end, we transfected different amount of plasmids into cell and examined the distribution of GFP-Lamin A (Fig. 3e). Interestingly, we observed foci formation of wild type GFP-Lamin A at high transfection dose, although, which was much less than R527C mutant Lamin A (Fig. 3e). This could be result from that the amount of endogenous BAF and LAP2 α was not enough to maintain the proper structure of overexpression wild type Lamin A. We then co-transfected BAF, LAP2 α and GFP-Lamin A into cells. BAF and LAP2 α were able to reduce the foci formation of wild type GFP-Lamin A but not R527C mutant (Fig. 3h,i). In line with this, knockdown of *BANF1* and *LAP2* promoted foci formation of wild type but not mutant GFP-Lamin A (Fig. 3j,k). Moreover, FLIP assay showed the fluorescence of wild type GFP-Lamin A was not able to be recovered as quickly and effectively as R527C mutant after photobleaching (Fig. 3f,g). Thus, Lamin A tended to aggregated and form foci due to its binding to BAF and LAP2 α was disrupted after R527C mutation (Fig. 3l). Consistently, similar protein aggregation was observed between wild type and mutant Lamin A (Fig. 2a). Moreover, wild type and mutant Lamin A exhibited similar capability to form droplet and filament in vitro (Extended Data Fig. 2a). Therefore, R527C mutation did not affect the ability of Lamin A to aggregate and form foci in vitro. This mutation promoted aberrant aggregation of protein in cells due to impaired binding ability to BAF and LAP2 α .

R527C mutation damps the interactions between Lamin A and LADs

Lamin A interacts with large chromatin domains referred to as Lamina-Associated Domains (LADs) that are distributed throughout the genome and are involved in genomic organization, epigenetic modifications, and regulation of gene expression. To determine if R527C mutation affect the arrangement and function of LADs, we performed Lamin A ChIP-seq and DamID-seq with wild type and mutant cell (Fig. 4a). Reads of Lamin A ChIP-seq and DamID-seq in LADs were decreased in mutant cells compared

with wild type (Fig. 4b and Extended Data Fig. 4a). These data suggested that the binding affinity of Lamin A to LADs was reduced after R527C mutation, which is consistent with our above results that mutant Lamin A failed to interact with DNA binding proteins, including BAF and LAP2 α (Fig. 2). Lamin A ChIP-seq showed that 317 (78.5%) LADs were lost, 14 (3.5%) LADs were gained, the reads of 41 (10.1%) LADs were decreased, and 3 (0.7%) LADs were increased (Fig. 4c). Cheedipudi et al. demonstrated that LADs were distributed across heterochromatic, promoter, and actively transcribed regions of the genome and were associated with DNA methylation and suppressed gene expression⁶³. We thus performed ATAC-seq to examine to chromatin of openness of coding genes. Unexpectedly, the reduction of LADs did not increase the accessibility of the promoters flanking coding genes. The genome wide analysis of ATAC-seq showed that openness of coding genes related chromatin was decreased in mutant MSCs (Fig. 4d). Consistently, the expression of according genes was downregulated (Fig. 4e). Thus, R527C mutant Lamin A showed lower affinity to LADs, which led to dysfunction of LADs and dysregulation of gene transcription, probably, leading to slow down or arrest of cell proliferation and differentiation.

Hyperactivation of cGAS-STING pathway in R527C MSCs

We above found that the patients with R527C mutant Lamin A showed autoimmune symptoms. Inflammatory genes, including a panel of interferon stimulated genes, were significantly upregulated in R527C mutant cells but not in G608G cells. Moreover, R527C Lamin A failed to bind to DNA binding protein, including BAF. A recent study showed that BAF restricts cGAS on nuclear damaged DNA to prevent innate immune activation⁶⁴, which promoted us to investigate that if cGAS was involved in the pathogenesis of this atypical progeria syndrome. We reconstituted wild type and R527C mutant FLAG-Lamin A into *LMNA* knockout HeLa cells, and reconstituted FLAG-progerin into wild type HeLa cells (Extended Data Fig. 5a). Comet assay showed that much more damaged DNA was detected in R527C mutant and progerin expressed cell than that in wild type cell (Fig. 5a). It is known that damaged DNA was able to activate cGAS pathway. However, interestingly, cGAS was activated and formed foci in R527C mutant but not in progerin expressed or wild type cells (Fig. 5b and Extended Data Fig. 5b). In line with this, increased cGAMP was detected in R527C mutant cells (Fig. 5c). Interestingly, *BANF1* knockdown promoted cGAS foci formation in progerin expressed cell but not wild type cell (Fig. 5b and 5d). Consistently, more cGAS was recruited to damaged DNA in R527C mutant cells than progerin expressed or wild type cells (Fig. 5e). We above found that progerin but not R527C mutant was able to interact with BAF (Fig. 2h). Thus, Lamin A might be required for protecting damaged DNA from cGAS by interacting with BAF. R527C mutant Lamin A failed to bind to BAF making damaged DNA exposure to cGAS.

It is believed that MSC enter senescence after a certain number of cell divisions⁶⁵. We thus measured the viability of wild type and R527C mutant MSCs at different passages (Fig. 5f). R527C mutant MSCs showed more significant proliferation arrest than wild type cells after 5 days. We treated these cells with STING inhibitor C-176, which could block activation of cGAS-STING pathway (Extended Data Fig. 5c). C-176 significantly increased the viability of both wild type and mutant MSCs leading to similar growth curves of these two kinds of cells (Fig. 5f). Further, we generated R527C mutant mice and isolated mouse

embryonic fibroblast (MEFs), bone marrow derived macrophages (BMDMs) and peritoneal macrophages (Fig. 5g). Consistent with above data, more damaged DNA was detected in Lamin A R527C mutant cells (Extended Data Fig. 5d-f). All of the mutant cells showed more severe senescence than wild type cells (Fig. 5h,i). Moreover, the senescence of BMDMs and peritoneal macrophages was able to be rescued by C-176 (Fig. 5i). Thus, cellular senescence could be rescued by inhibiting inflammation, indicating aberrant activation of innate immunity could be the cause or the driven force of aging caused by R527C mutation. Together, R527C mutation not only caused DNA damage but also damped the DNA protective function of BAF by disconnecting BAF from Lamin A, and consequently liberated cGAS-STING mediated inflammation.

Lmna^{R527C/R527C} mice exhibit elevated inflammation but no typical premature aging symptoms

We then investigated the mechanism by which R527C mutation caused accelerated aging in mice model. However, different from significant symptoms in human patients, we did not observe such differences between the mutant mice and wild type mice (Fig. 6a). Although the body weight of mutant mice was much less than wild type mice (Fig. 6b). The mutant mice did not die at the early age as human patients, and showed similar length of telomere to wild mice (Fig. 6c). The motility of mutant mice was similar to wild type mice even after two years old (Extended Data Fig. 6a). It is known that most of the *LMNA* R527C mutant patients and HGPS patients dead from heart failure⁶⁶. Echocardiography and HE staining showed that the function and structure of mutant mice were as normal as wild type mice (Fig. 6d,f and Extended Data Fig. 6b). Moreover, we did not observe decreased subcutaneous fatty tissue and gonad white adipose tissue (gWAT) inflammation (Fig. 6e,g and Extended Data Fig. 6c). We then examined if *Lmna*^{R527C/R527C} mice developed more inflammation than wild type mice in other tissues. RNA-seq analysis of the RNA from spleen showed that immune related genes were upregulated in mutant mice compared with wild type mice (Fig. 6h-j). Consistently, neutrophils were increased in the blood of mutant mice indicating that inflammation was activated (Fig. 6k and Extended Data Fig. 6d,e). It has been a Long-awaited question that activation of innate immunity is the cause or consequence associated with this in progression of aging. We here found that R527C mutation provoked inflammation before aging.

As mice were grew up in the animal facility without contact with the different environmental factors which were existed in patients' childhood constantly, including infection, nutrition diversity, irradiation and others. We thus tried to treat the mice with these factors and induce accelerated aging in mice, which would be useful for investigating the R527C *LMNA* mutation related premature aging. Ionizing radiation (IR) is a well-known inducer of oxidative stress and DNA damage, which are important factors for promoting the aging process. Thus, mutant and wild type mice were irradiated at 6 weeks of age with doses of 4 Gy, a regular protocol for inducing aging (Fig. 6l). Unexcepted, all the wild mice were in good condition, however, half of the mutant mice were dead within first month before developing aging (Fig. 6m). Similar to above data, more inflammation was detected in mutant mice than wild type mice after irradiation (Fig. 6o,p). Although the telomeres of mutant mice were significantly shorter than that of wild type at 10 months after irradiation (Fig. 6n). As most of the mice were dead within first month after

irradiation. A more moderate challenge should be applied to R527C mutant mice for investigating premature aging.

HFD causes premature aging of *Lmna*^{R527C/R527C} mice in a DNA sensing pathway dependent manner

We above found increased inflammation in *Lmna*^{R527C/R527C} mice (Fig. 6h-k) and DNA damage and cGAS-STING activation in mutant human cells (Fig. 5). To investigate if cGAS mediated the enhanced inflammation in mutant mice, we crossed *Lmna*^{R527C/R527C} mice with *Cgas*^{-/-} mice to generate double mutant mice. Interestingly, the increase of neutrophils and leucocytes in the blood was significantly reduced due to knockout of cGAS from R527C mutant mice (Fig. 7a). In line with this, the expressions of neutrophil marker gene and inflammatory mediators were remarkably down regulated in the spleen from double mutant mice compared with R527C mutant mice (Fig. 7b and Extended Data Fig. 7a). cGAS is the DNA sensor that activates inflammatory response by activating STING and initiating transcription of immune genes. AIM2 is another DNA sensor that activates inflammasome and promotes maturation and secretion of proinflammatory cytokines⁴⁸⁻⁵¹. To confirm the role of DNA sensing in R527C caused inflammation, we also crossed *Aim2*^{-/-} mice with R527C mutant mice. Consistent with cGAS deficient data, AIM2 deficiency greatly suppressed the increase of neutrophils and immune responses (Fig. 7a,b and Extended Data Fig. 7a). More strikingly, deficiency of cGAS or AIM2 was able to completely rescue the senescence of MEFs at high passage (Fig. 7c). Thus, these data suggested that DNA sensing pathways were responsible for the inflammation in R527C mutant mice and the senescence of mutant cells. However, the mice did not develop premature aging after mutation (Fig. 6).

It has been reported that high saturated fat diet (HFD)-induced inflammatory cytokine expression was enhanced in old mice⁶⁷. Moreover, HFD consumption has been shown to sensitize the inflammatory response to immune challenges⁶⁸. HFD could be a moderate challenge to enhance inflammation in mice. We thus fed wild type and R527C mutant mice with HFD (Fig. 7d). The body weight of wild type mice increased significantly. However, different from the result of normal diet feeding (Fig. 6b), mutant mice fail to gain the weight after HFD feeding (Extended Data Fig. 7b). Some of them started to lose the weight at day 70 after HFD feeding (Fig. 7e). More interestingly, mutant mice started to die at 3 months after HFD feeding. More than half of the mutant mice were dead at 8 months after HFD feeding. However, all the wild type mice were survived (Fig. 7f). In line with the survival results, the telomere of mutant mice became much shorter than wild type mice at 200 days after HFD feeding (Fig. 7g). Similar to the data of normal diet feeding, the number of neutrophils was increased in mutant mice with HFD feeding, and the difference was more significant suggesting more robust inflammation was activated (Fig. 7h). Echocardiography and HE staining showed that mutant mice developed typical symptoms of heart failure (Fig. 7i,j and Extended Data Fig. 7c), which was consistent with clinical features of *LMNA* R527C mutant patients and probably the culprit resulting in death of mice. Moreover, decreased subcutaneous fatty tissue and inflammation were also observed in mutant mice with HFD feeding (Fig. 7k and Extended Data Fig. 6d). These data suggested that HFD feeding was a good model that caused premature aging in mutant but not wild mice. Strikingly, knockout of *Aim2* was able to completely rescue the death of mutant

mice with HFD feeding (Fig. 7l). Consistently, telomere shortening and neutrophil increased was also significantly suppressed by the deficiency of AIM2 (Fig. 7m,n and Extended Data Fig. 7e,f). Together, DNA sensing innate immune pathways directed the inflammation and accelerated aging in *Lmna*^{R527C/R527C} mice.

Discussion

Inflammation is a hallmark of aging and accelerated aging syndromes. HGPS is a well characterized premature aging syndrome, whose pathophysiology has been associated to aberrant inflammatory responses⁶⁹. cGAS, a PRR, recognizes DNA from invading pathogens and naked endogenous double strands DNA. It has been claimed that cGAS senses damaged DNA and promotes inflammatory responses in the pathogenesis of HGPS. However, to our best knowledge, there is no experimental evidence showed that HGPS mutations causes activation of cGAS pathway. The description about cGAS and HGPS appeared in 21 literatures totally. 11 of them were review papers. Among the 10 research articles, only 3 of them clearly described the relationship between HGPS and cGAS. Firstly, Nuria Coll-Bonfill et. al. claimed that calcitriol prevents RAD51 Loss and cGAS-STING-IFN response triggered by progerin. However, they utilized a doxycycline-inducible GFP-progerin expression construct to monitor the effects of progerin induction, but not the mutated cells from patients⁷⁰. More importantly, they observed induction of cGAS and STING, and phosphorylation of STAT1, which were not direct experimental evidence to showed the activation of cGAS-STING pathway. The production of secondary messenger cGAMP and dimerization of STING should be examined to evaluate activation of cGAS-STING signaling. Secondly, from the same group, they found doxycycline-inducible progerin expression increases markers of DNA damage (γH2AX) and RS (P-RPA), global levels of PRRs, including cGAS and STING (DNA sensors), and RIG-I and OAS1 (RNA sensors). They did not determine the production of cGAMP or dimerization of STING. Thirdly, Xiaodong Mu et. al. claimed that cGAS-STING was activated by cytoplasmic chromatin in *Zmpste24*^{-/-} (*Z24*^{-/-}) mouse (a model for HGPS) and human HGPS fibroblasts. They only showed the increased expression of cGAS at protein level. As cGAS is an interferon stimulated gene. These data were not able to support the point that cGAS-STING was activated. Together, so far, there is no direct evidence showed cGAS-STING was activated in HGPS cells. We here examined the activation of cGAS in *LMNA* R527C mutated cells from patients. Foci of cGAS was detected and cGAMP production was significantly increased in *LMNA* R527C mutated cells than control cells. The level of cGAS was comparable between wild type and *LMNA* G608G mutated cell.

It is known that Lamin A is important for damage repair. Dysfunction of Lamin A cause accumulation of damaged DNA. Indeed, we here found that mutation G608G and R527C of *LMNA* resulted in comparable DNA damage. The damaged DNA was able to activate cGAS-STING pathway. However, R527C but not G608G mutation resulted in production of cGAMP, which is consistent with RNAseq data that R527C mutation provoked more significant immune responses (Fig. 1h,l). Lamin A function as a scaffold that ensures nuclear function such as DNA replication, transcription, and DNA repair⁷¹. It is known that Lamin A forms a ternary complex with BAF and Emerin, which promotes DNA repair⁷². Lamin A is critical for

recruiting and organizing DNA repair factors, including BAF. Our co-immunoprecipitation assay showed that R527C but not G608G mutation disrupted the binding of Lamin A to BAF (Fig. 2h). A recent study showed that BAF was able to protect DNA from sensing by cGAS. Although both R527C and G608G mutation caused severe DNA damage in the cell (Fig. 5a). cGAS was not able to sense damaged DNA in G608G mutation cells, but activated in R527C mutation cells due to lacking the ability to recruit BAF to damaged DNA. Thus, in addition to DNA damage, Lamin A regulate DNA sensing in a BAF dependent manner.

R527C mutation of *LMNA* cause premature aging in human. To investigate the mechanism of this atypical progeria *in vivo*, we generated *Lmna* R527C mutation mice. Interestingly, the cells from mutation mice underwent cellular senescence (Fig. 5g-i). However, the mice did not develop premature aging (Fig. 6a-g). This physiological difference between patients and mutant mice could resulted from different environmental condition, diet, immune system or other factors. A low-grade sterile chronic inflammation, has been described as a progressive event during biological ageing⁷³. We induced a low-grade sterile chronic inflammation to promote aging of mice by HFD feeding. Moreover, the mutant mice but not wild type mice developed enhance inflammation and accelerated aging after HFD feeding (Fig. 7d-k). Most of mice dead from heart failure within 8 months, which could be rescued by knockout of DNA sensor AIM2. Combine with the fact that mutant mice only developed overt inflammation but of aging, this AIM2 deficiency data further confirmed aberrant activation of innate immunity not only a progressive event but a major caused of premature aging. Therefore, the spontaneous inflammation caused by R527C mutation and additional inflammation from HFD made the mice to reach a threshold liberating development of premature aging. However, it is still unknown how HDF feeding trigger the aberrant inflammatory responses and accelerated aging in *LMNA* R527C mutant mice. Moreover, this HDF induced aging could be an ideal mice model to investigate the relationship between inflammation and aging *in vivo*. Taken together, we demonstrated that R527C mutation of Lamin A damped its interaction with a panel of DNA binding proteins and activated DNA sensing pathways, which led to overt inflammation and accelerated aging.

Declarations

Acknowledgements

This work was supported by the National Key Research and Development Program of China (2016YFA0500300, 2020YFA0707500 and 2020YFA0707800), the Strategic Priority Research Program (XDB29010000) and the National Natural Science Foundation of China (31570891; 31872736). Qinghua Zhou was supported by National Key R&D Program of China (2021YFA0804900) and the National Natural Science Foundation of China (NSFC 32170772). Wei Shu was supported by National Natural Science Foundation of China (32060157).

Author Contributions

F.Y., Q.Z., X.G. and G.Z. conceived the study and analyzed the data. Y.Z. performed most experiments and analyzed the data. W.S. analyzed all the clinical information and performed the PBMCs RNA-seq experiments. X.G., X.L. and X.J. optimized and performed the *LMNA* protein in vitro purification experiment. Q.Z. and J.L. built the *Lmna*^{R527C/R527C} mice. G.Z. and T.L. built the PBMC-derived iPS cells. Z.Z. and X.-F.G. analyzed all the high-throughput sequencing data. W.T. and X.S. optimized and performed the cGAMP mass spectrometry experiments. W.D. optimized and performed the ultrasonic echocardiography experiment in mice. M.K., H.D., Z.-M.Z., Z.-H.Z., X.W., D.W., T.-T.L., Y.L., S.L., J.C., Y.L., H.X. and L.C. supported on literature search and experiment performance. F.Y. wrote and revised the paper.

Declaration of Interests

The authors have no conflicts of interest to declare.

Data and Code Availability

The datasets generated during this study are available at Gene Expression Omnibus (<https://www.ncbi.nlm.nih.gov/geo/>). The accession number for the original high-throughput sequencing data reported in this paper is GEO: GSE190200.

Methods

Patient material, ethics and consent for publication

The blood samples and epidermal tissue samples used in this study from patients and healthy donors were preprocessed in a standardized manner and were collected with written informed consent. Relevant experiments were approved by medical ethic committee (Shenzhen Medical Ethics Committee, Shenzhen Luohu People's Hospital Medical Ethics Committee). Consent included the use of all de-identified patient data for publication. Participants were not compensated. Detail information of patients' family and healthy donors were listed in Table S1.

Generation of human PBMC derived-induced pluripotent stem cells

Blood samples were collected from patients and healthy donors. PBMCs from blood samples were isolated by density-based centrifugal separation. PBMCs were grown in Stem Pro-34 (Gibco, 10639-011) SFM complete medium containing SCF (SinoBiological, 10451-H08B), IL-3 (SinoBiological, 11858-HNAE), and GM-CSF (Peprotech, AF-315-03) for 12 days, and 2×10^6 of PBMCs were electroporated with iPSC

Reprogramming Vectors. After transfection, PBMCs were plated onto Matrigel-coated (Corning, 354277) 6 well culture-plates, and incubated in complete Stem Pro-34 medium containing cytokines for one day, N2B27 medium supplemented with 100 ng/ml bFGF (SinoBiological, 10014-HNAE) for one week, and finally Essential medium (Gibco, A15169-01) for two weeks. Colonies of iPSCs were manually picked 15–21 days after transfection, and transferred onto fresh Matrigel-coated 6 well culture-plates for expansion. iPSCs were passaged by 0.5mM EDTA for 8 min at 37 °C. iPSCs were split at 1:10 twice a week, and the cells were cultured in hPSC medium (Nuwacell, RP01001) at 37 °C in 5% CO₂.

Generation of mesenchymal stem cells from human induced pluripotent stem cells

When iPSCs were 20% confluent, hPSC medium was replaced with a series of MSC differentiation Basal Medium (Nuwacell, RP01013). After 14 days in culture, cells were considered as passage 0. iMSCs were passaged by MSC Solase for 5 min at 37 °C, and were seeded 5000 cells/ml in hMSC medium (Nuwacell, RP02010) at 37 °C in 5% CO₂. Further experiments were performed after flow cytometry analysis of MSC phenotypic characteristics at passage 4 (5×10^5 MSCs were incubated with 1% BSA for 30 minutes. The following antibodies were used: CD29-PE, CD34-APC, CD44-FITC, CD45-FITC, CD73-PE, CD90-PE, CD105-FITC, CD133-PE, CD146-PE, and HLA-DR-PE (BD Biosciences).

Cell culture

HEK293T cells and Hela cells were maintained in our lab. HEK 293T cells and Hela cells were cultured in DMEM medium supplemented with 10% FBS (PAN, ST30-3306), 100 U/mL Penicillin-Streptomycin at 37 °C in 5% CO₂. Cells were negative for mycoplasma.

Wild type / *Lmna*^{R527C/R527C} bone-marrow derived macrophages (BMDMs), peritoneal macrophages and *Lmna*^{WT/R527C} / *Lmna*^{R527C/R527C} mouse embryonic fibroblasts (MEFs) was isolated from mice.

Peritoneal macrophages were obtained from lavage of the peritoneal cavity with RPMI 1640 medium and were centrifuged and resuspended and cultured in indicated culture medium. For BMDMs, bone marrow cells were isolated from femurs and tibiae of 8-12 weeks old mice. Cells were cultured with 20 ng/mL recombinant murine GM-CSF (Peprotech, AF-315-03) in a 10-cm dish for 7 d before experiments. Mature macrophages were harvested by incubating with PBS-EDTA for 10 min and cultured in RPMI 1640 medium supplemented with 10% FBS, 100 U/mL Penicillin-Streptomycin at 37 °C in 5% CO₂.

MEFs were generated from embryonic day 13.5 (E13.5) embryos of *Lmna*^{WT/R527C} and *Lmna*^{R527C/R527C} mice under the normal culture condition, and were cultured in DMEM medium supplemented with 10% FBS, 100 U/mL Penicillin-Streptomycin at 37 °C in 5% CO₂.

CRISPR-Cas9 System

LMNA KO, *BANF1* KO, *LAP2* KO Hela cells and *Cgas* KO, *Aim2* KO MEF cells were constructed by CRISPR-Cas9 system. Specific guide RNAs (Table S2) were ligated into the BsmB1 restriction site of the inducible

lentiviral vector (lentiCRISPR v2). Lentivirus particles were produced by co-transfected HEK293 cells with guide RNA plasmids (2mg), packaging plasmids pCMV-VSV-G (800ng) and psPAX2 (800ng). The medium was changed to fresh DMEM containing 10% FBS at 6 h post transfection and viral supernatant was collected at 48 h. Then, target cells were infected with 1 mL viral supernatant or directly transfected with guide RNA plasmid. Possible knockout cells were screened by puromycin (Gibco, A1113803) and each monoclonal was confirmed by sequencing if necessary. The specific guide RNA sequences were as listed in Key Resource. HEK293 cells were transfected by standard polyethylenimine (Polysciences, 02371) precipitation method.

Generation of stable cell lines

LMNA KO HeLa cells stably expressing GFP-Lamin A, GFP-Lamin A(R527C), Flag-Lamin A, Flag-Lamin A(R527C), Dam-Lamin A, Dam-Lamin A(R527C), and HeLa cells stably expressing Flag-progerin were generated as follows. Specific protein coding sequences were ligated into the inducible lentiviral vector (pCDH-CMV-MCS-EF1 α -puro). Lentivirus particles were produced by co-transfected HEK293 cells with reconstructed plasmids (2mg), packaging plasmids pCMV-VSV-G (800ng) and psPAX2 (800ng). The medium was changed to fresh DMEM containing 10% FBS at 6 h post transfection and viral supernatant was collected at 48 h. Then, target cells were infected with 1 mL viral supernatant and incubated for 48 h. Possible knockout cells were screened by puromycin and each monoclonal was confirmed by sequencing if necessary. HEK293 cells were transfected by standard polyethylenimine precipitation method. All stable cell lines were used at early passages in experiments.

Mice and In Vivo experiments

All animals care and use adhered to the Guide for the Care and Use of Laboratory Animals of the Chinese Association for Laboratory Animal Science. All procedures of animal handling were approved by the Animal Care Committee of Peking University Health Science Center.

Wild type C57BL/6J mice were purchased from Department of Laboratory Animal Science of Peking University Health Science Center, Beijing. *Cgas*^{-/-} mice and *Aim2*^{-/-} mice on a C57BL/6J background were gift from Pro. Zhengfan Jiang (Peking University). The *Lmna* R527C mutant mice (C57BL/6) were generated by Cyagen Biosciences using the CRISPR/Cas9 system. *Cgas*^{-/-}*Lmna*^{R527C/R527C} mice and *Aim2*^{-/-}*Lmna*^{R527C/R527C} mice were generated by *Lmna*^{R527C/R527C} mice bred with *Cgas*^{-/-} mice and *Aim2*^{-/-} mice. Mice were kept and bred in specific pathogen-free conditions under controlled temperature (23 ± 1°C) and exposed to a constant 12 h light-dark cycle. All animals are guaranteed adequate clean water and nutritious feed. The primers for genotyping were as listed in Table S2

Age- and sex-matched C57BL/6 littermates were produced and used in all the in vivo experiments. For irradiation mice model, Wild type and *Lmna*^{R527C/R527C} 6-week-old male mice were treated by 4 GY irradiation. Blood was collected at day -1 and day 7 post-irradiation for hemanalysis, genome DNA was collected at day -1 and day 300 post-irradiation for telomere length analysis. Mice were sacrificed at day

-1 and day 7 post-irradiation and spleen was harvested for RT-PCR analysis and RNAseq, or mice were monitored survival and body weight change daily. For high-fat-diet mice model, wild type, *Lmna*^{R527C/R527C}, and *Aim2*^{-/-}*Lmna*^{R527C/R527C} 6-week-old male mice were fed with normal chow or high-fat diet (Research Diets, D12492). Blood and genome DNA were collected at month 0, month 1, month 3, month 5, and month 7 after normal chow or high-fat diet for hemanalysis and telomere length analysis. Mice were monitored survival and body weight change daily. Echocardiographic analysis was performed at month 8, and then mice were sacrificed and tissues were harvested for HE staining analysis.

Constructs

Expression constructs generated for this study were prepared by standard molecular biology techniques and coding sequences entirely verified. All the truncations deletions and mutants were constructed by standard molecular biology technique. Each truncation, deletions and mutants were confirmed by sequencing. The constructs used were as listed in Table S3.

Protein expression and purification

The gene coding for wild type or R527C mutant Lamin A were cloned into the pET21d vector. Plasmids were transformed into *E. coli* BL21(DE3) for expression. Strains carrying the different plasmids were grown to an OD_{600nm} of 0.6–0.7 at 37 °C, expression of wild type or mutant Lamin A protein was subsequently induced by the addition of 0.5 mM IPTG, and further incubated overnight at 20°C. Bacterial cells were pelleted by centrifugation, and resuspended in lysis buffer (20mM Tris-HCl, pH8.0 and 150 mM NaCl) supplemented with 1mM PMSF, 100µg/ml Dnase (New England Biolabs, M0303) and 100µg/ml lysozyme. After cells were lysed using a high-pressure cell disrupter and the pellets were collected by centrifugation at 17,000 × g for 20min. The pellets were incubated in a buffer containing 20mM Tris-HCl, pH8.0, 150mM NaCl, 8M Urea at room temperature for 30min, the supernatants collected after centrifugation (17000 × g, 20min) were further purified by HiTrap Q HP ion-exchange and Superdex 200 gel filtration chromatography under denature condition (with 8M Urea always in the buffer). The purified protein was dialysis against suitable buffer for refolding as needed before use.

Turbidity Assay

0.8 mg/mL wild type or R527C mutant Lamin A protein were mixed in 150 mM NaCl, 1mM EDTA, 1mM DTT and 25mM Tris-HCl/MES with various PH (PH=6.0/6.5/7.0/7.4). Sample were incubated at room temperature for 30 minutes prior to the absorption (turbidity) measurement at 600nm by FlexStation 3. Readings were recorded in triplicate for each protein sample. All assays were performed in triplicate.

Droplet Assay

0.8 mg/mL wild type or R527C mutant Lamin A protein were mixed in 150 mM NaCl, 1mM EDTA, 1mM DTT and 25mM Tris-HCl/MES with PH=6.5. Samples were deposited on 8-well glass bottom Ibidi slides,

then samples were incubated at room temperature and were imaged on microscope. Droplet and fiber formation were observed over time.

Antibodies and Beads.

Commercially available antibodies against the following proteins were used in this study. Mouse antibodies: Lamin A/C (Abcam, ab8980), DYKDDDDK tag (Proteintech, 66008-3-Ig), and GAPDH (Proteintech, 60004-1-Ig). Rabbit antibody: Lamin A/C (Proteintech, 10298-1-A), HA tag (Proteintech, 51064-2-AP), DYKDDDDK tag (Proteintech, 20543-1-AP), cGAS (Cell Signaling Technology, 15102), beta Tubulin (Proteintech, 10094-1-AP), Lamin B (Proteintech, 12987-1-AP), GFP tag (Proteintech, 50430-2-AP), and γ H2A.x (Cell Signaling Technology, 9817). HRP-conjugated secondary antibodies (goat anti-mouse IgG and goat anti-rabbit IgG) were purchased from Proteintech. Alexa Fluor 488 or 555-conjugated secondary antibodies (donkey anti-mouse IgG and donkey anti-rabbit IgG) were purchased from Invitrogen.

Western blot analysis

Whole-cell extracts were prepared using RIPA lysis buffer (50 mM Tris, pH 7.4, 150 mM NaCl, 1% NP-40, 0.1% SDS, and 0.5% deoxycholate, supplemented with a protease inhibitor (TargetMol, B14001) and centrifuged at 10,000 g for 10 min at 4 °C. Proteins were resolved on 10% SDS-PAGE and transferred onto nitrocellulose membranes. Blocked membranes were incubated with the primary antibodies for 1 h at 37 °C. Secondary antibodies conjugated to HRP and Western Chemiluminescent HRP Substrate were used for detection.

Immunofluorescence Microscopy

Different treatments and genotypes of HeLa cells, MSCs, BMDMs and peritoneal macrophages on coverslips were washed twice with pre-warmed phosphate buffered saline (PBS) and fixed in 4% (wt/vol) paraformaldehyde for 10 min. After three washes in PBS, cells were permeabilized with 0.5% (vol/vol) Triton X-100 for 5 min. After three washes in PBS, cells were blocked in PBS containing 1% (wt/vol) bovine serum albumin (BSA) for 60 min, and incubated with indicated antibodies in PBS containing 1% (wt/vol) BSA for 1 h at 37 °C. After three washes, cells were incubated with Alexa Fluor 488-conjugated secondary antibodies or Alexa Fluor 555-conjugated secondary antibodies for 1 h at 37 °C, and then with DAPI (40,6-Diamidino-2-phenylindole; Invitrogen, P36961) for 15 min. The coverslips were washed extensively and mounted onto slides. Imaging of the cells was carried out using N-STORM 5.0 microscope.

Quantitative RT-PCR (qRT-PCR) analysis

Total RNA was isolated from the tissues and cells by TRNzol reagent (TIANGEN Biotech, DP424). Then, cDNA was prepared using HiScript III 1st Strand cDNA Synthesis Kit (Vazyme Biotech, R312-02). qRT-PCR was performed using the Applied Biosystems 7500 Real-Time PCR Systems with SYBR qPCR Master mix

(Vazyme Biotech, Q331-02). The data of qRT-PCR were analyzed by the Livak method ($2^{-\Delta\Delta Ct}$). Beta-actin was used as a reference gene. The primers for qRT-PCR were as listed in Table S2.

RNA sequencing (RNA-seq)

Whole RNA of tissues and cells with specific treatments were purified using TRNzol reagent. The transcriptome library for sequencing was generated using VAHTSTM mRNA-seq v2 Library Prep Kit for Illumina (Vazyme Biotech, R312-02) following the manufacturer's recommendations. After clustering, the libraries were sequenced on Illumina HiSeq X Ten platform using (2 × 150 bp) paired-end module. The raw data were transformed into raw reads by base calling using CASAVA.

Luciferase Reporter Assay

HEK293T cells (2×10^5) were plated in 24-well plates and transfected using polyethylenimine, with pGL3-mlf1b-promoter plasmids (firefly luciferase; 10 ng) and pRL-TK (renilla luciferase plasmid; 10 ng) together with 100 ng pCMV-3×FLAG-7.1 or pCMV-3×Flag-STING plasmid. The medium was changed to fresh DMEM containing 10% FBS with DMSO or 100nM C176 (TargetMol, T5154) at 6 h post transfection. After transfection for 24 h, cells were lysed and luciferase activity was measured with the Dual-Luciferase Assay System (Promega, E1910) according to the manufacturer's instructions. Reporter gene activity was determined by normalization of the firefly luciferase activity to renilla luciferase activity.

Co-immunoprecipitation

HEK293 cells (1×10^7) were seeded on 10 cm² dishes and were transfected with a total of 10 ug of empty plasmid or various expression plasmids. The medium was changed to fresh DMEM containing 10% FBS at 6 h post transfection. After transfection for 24 h, cells were lysed in lysis buffer (0.5% Triton X-100, 20 mM HEPES (PH 7.4), 150 mM NaCl, 12.5 mM b-glycerolphosphate, 1.5 mM MgCl₂, 2 mM EDTA, 10 mM NaF, 1 mM Na₃VO₄, 2 mM DTT) containing protease inhibitors. Lysates were centrifuged and incubated with anti-Flag antibodies at 4 °C overnight. The next day, prewashed protein A/G beads (Thermo, 20422) were added and incubated at 4 °C for 4 h. The beads were washed with cold PBS 4 times and eluted with DTT-containing SDS sample buffer by boiling for 10 min for western blotting.

Histology and immunohistochemical staining

For H&E staining, mice tissues were quickly placed in cold saline solution and rinsed after they were collected. Then, tissues were fixed in 4% paraformaldehyde, dehydrated and embedded in paraffin prior to sectioning at 5 mm, and sections were stained with hematoxylin and eosin. Several H&E staining images were randomly selected for pathological scoring in a blinded fashion.

For immunohistochemical staining, the human epidermal tissues paraffin sections were dewaxed and rehydrated through xylene and an alcohol gradient. Antigen retrieval was performed by heating the sections to 100 °C for 4 min in 0.01 M citrate buffer (pH 6.0) and repeated 4 times. The operations were performed according to the instructions of the two-step detection kit. The samples were treated by

endogenous peroxidase blockers for 10 min at room temperature followed by incubation with Lamin A antibodies at 37 °C for 1 h. Then after washed with PBS, the samples were incubated with reaction enhancer for 20 min at room temperature and secondary antibodies at 37 °C for 30 min, and finally sections were visualized by 3,30-diaminobenzidine tetrahydrochloride (DAB) and counterstained with hematoxylin.

Telomere length detection

Total DNA was isolated from the tissues by Genomic DNA Extraction Kit (TIANGEN Biotech, DP304). Then, qRT-PCR was performed using the Applied Biosystems 7500 Real-Time PCR Systems with SYBR qPCR Master mix. The data of qRT-PCR were analyzed by the Livak method ($2^{-\Delta\Delta C_t}$). *36B4* was used as a reference gene. The primers for qRT-PCR were as listed in Table S2.

SA-β-gal staining

Control and patient-derived MSCs were washed twice in PBS, fixed for 3–5 min at room temperature in 3% formaldehyde, and washed with PBS again. Then cells were incubated overnight at 37 °C (without CO₂) with freshly prepared SA-β-gal stain solution (1 mg/ml X-gal, 40 mM citric acid/sodium phosphate, pH 6.0, 5 mM potassium ferrocyanide, 5 mM potassium ferricyanide, 150 mM NaCl, 2 mM MgCl₂) according to Senescence β-Galactosidase Staining Kit (Cell Signaling Technology, 9860). Positive staining appeared after 2–4 h and was evaluated after 12–16 h incubation at 37 °C in a CO₂-free atmosphere. The blue stained cells were monitored under the microscope.

Comet assay

Slides were prepared with 85 μl of 0.5% normal melting agarose. *LMNA* KO HeLa cells stably expressing Flag-Lamin A, Flag-Lamin A (R527C), and HeLa cells stably expressing Flag-progerin were then mixed with 75 μl of 0.5% low melting agarose and applied to the prepared slides. Alkaline lysis (10% DMSO, 1% Triton-X in alkaline lysis buffer: 2.5 M NaCl, 10 mM Tris, 100 mM Na₂EDTA, pH 10) followed for 1 h. Then slides were placed in a horizontal gel electrophoresis chamber containing alkaline buffer solution with NaOH (10 mM) and Na₂EDTA (200 mM) at pH 13.2. After a 20-min DNA “unwinding” period, electrophoresis was performed at 25 V and 300 mA for 20 min. Following neutralization (Tris-HCl, pH 7.5), the cells were stained with ethidium bromide (Invitrogen, 15585011). The slides were examined and the tail length (diameter of the nucleus plus migrated DNA) was measured with microscope. The DNA migration of 100 randomly selected cells was examined for each sample.

Fluorescence Recovery after Photobleaching (FRAP)

FRAP was performed with a N-STORM 5.0 microscope using the semiconfluent monolayer of live cells over slides covered with *LMNA* KO HeLa cells stably expressing GFP-Lamin A (wild type/R527C/1-390/1-425). The laser intensity and photobleaching duration were standardized to eradicate at least 80% of fluorescence. After two low laser intensity scans, circle areas in different cell regions were bleached using

a 488 laser at high intensity. Next, the bleached areas were scanned for 20 min using a low intensity laser. The fluorescence intensity in the obtained images was measured in the regions of interest (ROIs) using the ImageJ software. To calculate the ratio (R) between the time of half recovery in the cell–cell contacts and the free membrane, we used the formula: $R = (F_e - F_0)/(F_i - F_0)$, where F_e is the fluorescence at the end of the experiment, F_i is the fluorescence at the beginning, and F_0 is the fluorescence just after bleaching.

MEF Immortalization.

MEF Immortalization assay was conducted as described⁴⁸. MEFs were generated from embryonic day 13.5 (E13.5) embryos of *Lmna*^{WT/R527C} and *Lmna*^{R527C/R527C} mice under the normal culture condition that includes 20% oxygen and 5% CO₂. For spontaneous immortalization, we followed a modified 3T3 protocol by seeding 1×10^6 cells in a 10-cm dish every 3.5 d. Aliquots of the cells at indicated passages were expanded for continued passages, frozen in liquid nitrogen.

Hemanalysis

Mice blood was obtained at indicated day after irradiation or high-fat diet by a tail snip. 50 μ L blood was collected to heparin-coated tube and then was analyzed with HEMAVET 950 Analyzer.

Echocardiography

Two-dimensional M-mode echocardiography was performed on anesthetized mice using a Vevo2100 high-resolution imaging system with a 30-MHz high-frequency transducer to evaluate the cardiac function.

Cell viability assay

Wild type/*Lmna*^{R527C/R527C} BMDMs and peritoneal macrophages (1×10^7) were seeded into 10 cm² dishes and treated with or without 10 nM C176 for 1 month. **Cell viability** was examined using the Cell Counting Kit-8 assay (Bimake, B34302) according to the manufacturer's instructions. The Optical density (OD) values were measured at 450 nm by FlexStation 3. Each experiment was repeated at least three times.

Assay for Transposase-Accessible Chromatin sequencing (ATAC-seq)

Pellet 50,000 viable control and patient-derived MSCs at 500 RCF at 4°C for 5 min. Aspirate all supernatant. Add 50 μ L cold ATAC-Resuspension Buffer (RSB) containing 0.1% NP40, 0.1% Tween-20, and 0.01% Digitonin into the cell pellet and pipette up and down 3 times. Incubate on ice for 3 minutes. Wash out lysis with 1 mL cold ATAC-RSB containing 0.1% Tween-20 but no NP40 or digitonin and invert tube 3 times to mix. Pellet nuclei at 500 RCF for 10 min at 4°C. Aspirate all supernatant. Resuspend cell pellet in 50 μ L of transposition mixture (25 μ L 2x TD buffer, 2.5 μ L transposase (100 nM final), 16.5 μ L PBS, 0.5 μ L 1% digitonin, 0.5 μ L 10% Tween-20, 5 μ L H₂O) by pipetting up and down 6 times. Incubate reaction at 37 °C for 30 minutes. Afterward, the DNA was purified with QIAEX II Gel Extraction Kit (Qiagen,

20021) and amplified with primers containing barcodes by using the TruePrep DNA Library Prep Kit (Vazyme Biotech, TD501-01). All libraries were adapted for sequencing.

DamID library preparation and sequencing

The gDNA of Dam-Lamin A (wild type/R527C) stably expression *LMNA* KO Hela cells were ethanol-precipitated overnight at $-20\text{ }^{\circ}\text{C}$ and dissolved in Tris-EDTA (pH 7.5) to a concentration of 1 mg/ml. gDNA (2.5 ml) was digested with Dpn I (New England Biolabs, R0176) at 37°C overnight, and Dpn I was inactivated by heating to $80\text{ }^{\circ}\text{C}$ for 20 min. Dpn I-digested gDNA was ligated to the adaptor AdR by T4 Ligase. After enzyme was inactivated by heating to $65\text{ }^{\circ}\text{C}$ for 10 min, samples were digested by Dpn II (New England Biolabs, R0543) at $37\text{ }^{\circ}\text{C}$ for 1 hour. PCR reaction was performed to amplify the regions flanked by adaptors. The PCR products were cleaned with the QIAEX II Gel Extraction Kit. All libraries were adapted for sequencing. The primers for AdR were as listed in Table S2.

Chromatin Immunoprecipitation (ChIP)

Chromatin Immunoprecipitation was conducted as described⁷⁵. Approximately 5×10^7 pretreated cells were crosslinked with 1% formaldehyde at room temperature for 10 min, and the reaction was quenched with 0.125M glycine for 5 min. The cells were washed twice with PBS, then scrapped and pelleted at 2500 rpm for 5 min at $4\text{ }^{\circ}\text{C}$. After lysis and sonication, the majority of the sonicated DNA fragments were sheared to a size of around 200–600 bp. The sonicated chromatin was spun down at 12,000 rpm for 10 min at $4\text{ }^{\circ}\text{C}$ to collect the chromatin. Then the soluble chromatin was incubated with 3 mg antibody and the mixture were rotated at $4\text{ }^{\circ}\text{C}$ overnight. After incubation, pre-washed Protein G Dynabeads (Invitrogrn, 10004d) were added and incubated for 4 h at $4\text{ }^{\circ}\text{C}$ in a rotator. Then the magnetic Dynabeads were pelleted by placing the tubes in a magnetic rack and were washed for a total of five times: once with wash buffer A (20 mM Tris-HCl (pH 8.0), 500 mM NaCl, 2 mM EDTA, 0.1% SDS, 1% Triton X-100); once with wash buffer B (10 mM Tris-HCl (pH 8.0), 250 mM LiCl, 1 mM EDTA, 1%NP-40); three times with wash buffer C (1 mM EDTA, 10 mM Tris-HCl(pH 8.0)).

For sequencing, beads were resuspended in 100 mL elution buffer (50 mM Tris-HCl (pH 8.0), 10 mM EDTA, 1% SDS), followed by incubation at $65\text{ }^{\circ}\text{C}$ overnight for reverse crosslink. Purify DNA of input and Lamin A antibody immunoprecipitation samples from control and patient-derived MSCs with QIAEX II Gel Extraction Kit. The extracted DNA was used for sequencing.

For western blot analysis, the Replication Proteion A antibody beads which combined Replication Proteion A antibody were resuspended in $50\text{ }\mu\text{l}$ 1×SDS loading buffer containing 100 mM DTT followed by incubation at $100\text{ }^{\circ}\text{C}$ for 20 min. Input samples were added 4×SDS loading buffer containing 100 mM DTT followed by incubation at $100\text{ }^{\circ}\text{C}$ for 20 min.

Immunoprecipitation-Mass Spectrometry

Whole-cell extracts of control and patient-derived MSCs (3×10^7) were prepared using RIPA lysis buffer (50 mM Tris, pH 7.4, 150 mM NaCl, 1% NP-40, 0.1% SDS, and 0.5% deoxycholate, supplemented with a protease inhibitor tablet) and centrifuged at 10,000 g for 10 min at 4 °C. Lysis were centrifuged and incubated with anti-Lamin A antibodies at 4 °C overnight. The next day, prewashed protein A/G beads were added and incubated at 4 °C for 4 h. The beads were washed with cold PBS 4 times and eluted with 50 mM Tris-HCl (pH=7.5) by incubation at 100 °C for 10 min for mass spectrometry.

CGAMP Quantification by Mass Spectrometry

CGAMP Quantification by Mass Spectrometry was conducted as described ⁷⁶. Briefly, transfer the lysed cells in 300 μ L extraction reagent with internal standard. Incubate samples and prepared cGAMP (Sigma Aldrich, 5.31889) calibration solutions to 95 °C for 15 min and cool down on ice. Precipitate proteins of the cell lysates by incubating at -20 °C overnight. Subsequently, centrifuge at 20,000 \times g for 15 min to pellet down protein precipitates. Vaporize protein-free supernatants completely, and dissolve the pellet in 150 μ L HPLC-grade water. Vortex samples and transfer 75 μ L of the solution into the glass micro-inserts of the thread-bottles for HPLC-MS/MS measuring.

RNA-seq analysis

The FastQC and Trim Galore were used for raw data quality control, then the R package Rsubread ⁷⁷ was used for mapping and counting the reads. The count matrix was normalized by FPKM. The differentially expressed genes were identified by the GFOLD, a Linux software ⁷⁸. The GO annotations of DEGs were performed in the DAVID database (<https://david.ncifcrf.gov/home.jsp>).

ChIP-seq and DamID-seq Data Analysis

Reads from ChIP-seq and DamID-seq experiments were aligned to Human genome GRCh38 using annotated chromosomes and scaffolds. Alignment was performed using bowtie 2 ⁷⁹. Regions with an exceptionally high coverage of ChIP-Seq and DamID-seq reads were identified using MACS2 ⁸⁰. Wiggle files representing counts of ChIP-Seq and DamID-seq reads across the reference genome were created using MACS2. Resulting wiggle files were normalized for sequencing depth by dividing the read counts in each bin by the millions of mapped reads in each sample and were visualized in the UCSC genome browser (The human genome browser at UCSC, 2002) or WashU genome browser (The human epigenome browser at Washington University, 2011).

ATAC-seq Data Analysis

ATAC-seq reads were aligned using Bowtie 2 with the Human genome GRCh38. This was followed by peak calling on each replicate individually using MACS2 with the function “callpeak”. Peaks were classified (annotatePeaks.pl–annStats) as intronic, exonic, upstream or intergenic, according to the gene feature they intersected. Intersection is scored first considering the number of bases overlapped, and then the closeness in size between the peak and the feature. The height of the peaks, as well as any reads

outside the peaks, were quantified using bedtools⁸¹. The peak levels were divided by the background signal for normalization. The MACS2-generated files were visualized in the UCSC genome browser (The human genome browser at UCSC, 2002)

Statistical analysis

All analyses were repeated at least three times, and a representative experimental result was presented. Data were analyzed using GraphPad Prism version 8.0. Continuous variables with normal distribution are expressed as the mean \pm standard deviation (SD). Comparisons between groups were all verified for normal distribution by D'Agostino-Pearson omnibus test. Student's t-test (for pairwise comparisons) and one-way ANOVA (for comparisons among three or more groups) were used. The post hoc test with Bonferroni correction was performed for multiple comparisons following ANOVA. Asterisks denote statistical significance (*P < 0.05; **P < 0.01; *** P < 0.001). Data are shown as means \pm SD (n \geq 3).

References

1. Smith, E. D., Kudlow, B. A., Frock, R. L. & Kennedy, B. K. A-type nuclear lamins, progerias and other degenerative disorders. *Mech Ageing Dev* **126**, 447–460, doi:10.1016/j.mad.2004.10.006 (2005).
2. Peter, A. & Stick, R. Evolution of the lamin protein family. *Nucleus* **3**, 44–59, doi:10.4161/nucl.18927 (2012).
3. Stuurman, N., Heins, S. & Aebi, U. Nuclear lamins: their structure, assembly, and interactions. *J Struct Biol* **122**, 42–66, doi:10.1006/jsbi.1998.3987 (1998).
4. Broers, J. L. V., Ramaekers, F. C. S., Bonne, G., Yaou, R. B. & Hutchison, C. J. Nuclear Lamins: Laminopathies and Their Role in Premature Ageing. *Physiological Reviews* **86**, 967–1008, doi:10.1152/physrev.00047.2005 (2006).
5. Chojnowski, A., Ong, P. F. & Dreesen, O. Nuclear lamina remodelling and its implications for human disease. *Cell and Tissue Research* **360**, 621–631, doi:10.1007/s00441-014-2069-4 (2015).
6. Meaburn, K. J. *et al.* Primary laminopathy fibroblasts display altered genome organization and apoptosis. *Aging Cell* **6**, 139–153, doi:10.1111/j.1474-9726.2007.00270.x (2007).
7. Vlcek, S. & Foisner, R. Lamins and lamin-associated proteins in aging and disease. *Current Opinion in Cell Biology* **19**, 298–304, doi:10.1016/j.ceb.2007.04.001 (2007).
8. Mahen, R. *et al.* A-Type Lamins Maintain the Positional Stability of DNA Damage Repair Foci in Mammalian Nuclei. *PLoS ONE* **8**, e61893, doi:10.1371/journal.pone.0061893 (2013).
9. Singh, M. *et al.* Lamin A/C Depletion Enhances DNA Damage-Induced Stalled Replication Fork Arrest. *Molecular and Cellular Biology* **33**, 1210–1222, doi:10.1128/mcb.01676-12 (2013).
10. Gibbs-Seymour, I., Markiewicz, E., Bekker-Jensen, S., Mailand, N. & Hutchison, C. J. Lamin A/C-dependent interaction with 53BP1 promotes cellular responses to DNA damage. *Aging Cell* **14**, 162–169, doi:10.1111/accel.12258 (2015).

11. Broers, J. L. *et al.* A- and B-type lamins are differentially expressed in normal human tissues. *Histochem Cell Biol* **107**, 505–517, doi:10.1007/s004180050138 (1997).
12. Liu, G.-H. *et al.* Recapitulation of premature ageing with iPSCs from Hutchinson–Gilford progeria syndrome. *Nature* **472**, 221–225, doi:10.1038/nature09879 (2011).
13. Hetzer, M. W. The Nuclear Envelope. *Cold Spring Harbor Perspectives in Biology* **2**, a000539–a000539, doi:10.1101/cshperspect.a000539 (2010).
14. Kochin, V. *et al.* Interphase phosphorylation of lamin A. *Journal of Cell Science* **127**, 2683–2696, doi:10.1242/jcs.141820 (2014).
15. Fatkin, D. *et al.* Missense mutations in the rod domain of the lamin A/C gene as causes of dilated cardiomyopathy and conduction-system disease. *N Engl J Med* **341**, 1715–1724, doi:10.1056/NEJM199912023412302 (1999).
16. Bonne, G. *et al.* Mutations in the gene encoding lamin A/C cause autosomal dominant Emery-Dreifuss muscular dystrophy. *Nat Genet* **21**, 285–288, doi:10.1038/6799 (1999).
17. Muchir, A. *et al.* Identification of mutations in the gene encoding lamins A/C in autosomal dominant limb girdle muscular dystrophy with atrioventricular conduction disturbances (LGMD1B). *Hum Mol Genet* **9**, 1453–1459, doi:10.1093/hmg/9.9.1453 (2000).
18. Shackleton, S. *et al.* LMNA, encoding lamin A/C, is mutated in partial lipodystrophy. *Nat Genet* **24**, 153–156, doi:10.1038/72807 (2000).
19. Cao, H. & Hegele, R. A. LMNA is mutated in Hutchinson-Gilford progeria (MIM 176670) but not in Wiedemann-Rautenstrauch progeroid syndrome (MIM 264090). *J Hum Genet* **48**, 271–274, doi:10.1007/s10038-003-0025-3 (2003).
20. Eriksson, M. *et al.* Recurrent de novo point mutations in lamin A cause Hutchinson-Gilford progeria syndrome. *Nature* **423**, 293–298, doi:10.1038/nature01629 (2003).
21. Novelli, G. *et al.* Mandibuloacral dysplasia is caused by a mutation in LMNA-encoding lamin A/C. *Am J Hum Genet* **71**, 426–431, doi:10.1086/341908 (2002).
22. Youn, G. J. *et al.* Autosomal recessive LMNA mutation causing restrictive dermopathy. *Clin Genet* **78**, 199–200, doi:10.1111/j.1399-0004.2010.01385.x (2010).
23. Chen, L. *et al.* LMNA mutations in atypical Werner's syndrome. *The Lancet* **362**, 440–445, doi:10.1016/s0140-6736(03)14069-x (2003).
24. Worman, H. J. & Bonne, G. "Laminopathies": a wide spectrum of human diseases. *Exp Cell Res* **313**, 2121–2133, doi:10.1016/j.yexcr.2007.03.028 (2007).
25. Muchir, A. & Worman, H. J. Emery-Dreifuss muscular dystrophy. *Current Neurology and Neuroscience Reports* **7**, 78–83, doi:10.1007/s11910-007-0025-3 (2007).
26. Taylor, M. R. *et al.* Thymopoietin (lamina-associated polypeptide 2) gene mutation associated with dilated cardiomyopathy. *Hum Mutat* **26**, 566–574, doi:10.1002/humu.20250 (2005).
27. Puente, X. S. *et al.* Exome sequencing and functional analysis identifies BANF1 mutation as the cause of a hereditary progeroid syndrome. *Am J Hum Genet* **88**, 650–656,

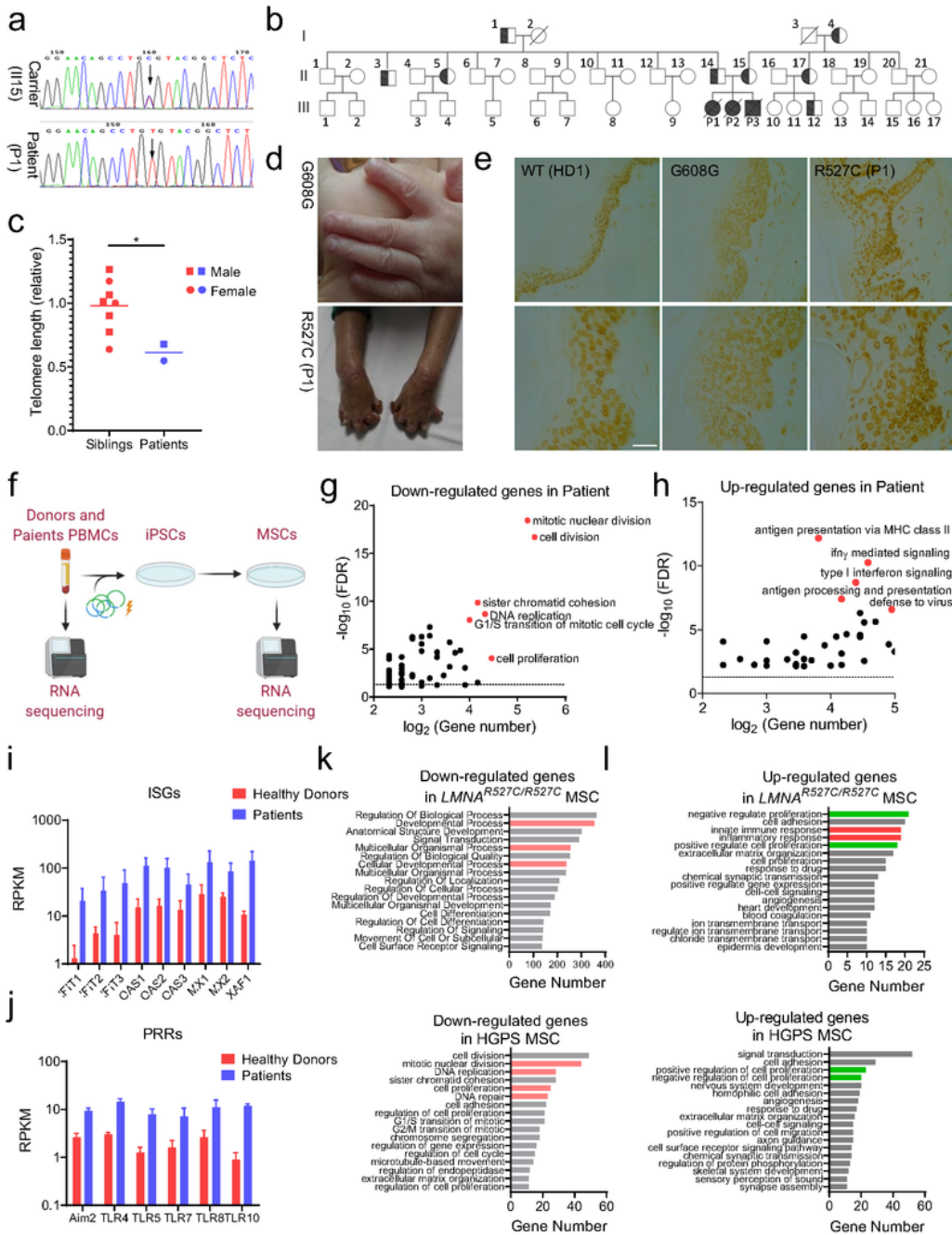
- doi:10.1016/j.ajhg.2011.04.010 (2011).
28. Pereira, S. *et al.* HGPS and related premature aging disorders: from genomic identification to the first therapeutic approaches. *Mech Ageing Dev* **129**, 449–459, doi:10.1016/j.mad.2008.04.003 (2008).
 29. Agarwal, A. K., Fryns, J. P., Auchus, R. J. & Garg, A. Zinc metalloproteinase, ZMPSTE24, is mutated in mandibuloacral dysplasia. *Hum Mol Genet* **12**, 1995–2001, doi:10.1093/hmg/ddg213 (2003).
 30. Worman, H. J., Ostlund, C. & Wang, Y. Diseases of the Nuclear Envelope. *Cold Spring Harbor Perspectives in Biology* **2**, a000760–a000760, doi:10.1101/cshperspect.a000760 (2010).
 31. Korf, B. Hutchinson–Gilford Progeria Syndrome, Aging, and the Nuclear Lamina. *New England Journal of Medicine* **358**, 552–555, doi:10.1056/nejmp0800071 (2008).
 32. Moulson, C. L. *et al.* Increased progerin expression associated with unusual LMNA mutations causes severe progeroid syndromes. *Hum Mutat* **28**, 882–889, doi:10.1002/humu.20536 (2007).
 33. Scharner, J., Lu, H.-C., Fraternali, F., Ellis, J. A. & Zammit, P. S. Mapping disease-related missense mutations in the immunoglobulin-like fold domain of lamin A/C reveals novel genotype-phenotype associations for laminopathies. *Proteins: Structure, Function, and Bioinformatics* **82**, 904–915, doi:10.1002/prot.24465 (2014).
 34. Soria-Valles, C. *et al.* Novel LMNA mutations cause an aggressive atypical neonatal progeria without progerin accumulation. *Journal of Medical Genetics* **53**, 776–785, doi:10.1136/jmedgenet-2015-103695 (2016).
 35. Van Esch, H., Agarwal, A. K., Debeer, P., Fryns, J.-P. & Garg, A. A Homozygous Mutation in the Lamin A/C Gene Associated with a Novel Syndrome of Arthropathy, Tendinous Calcinosis, and Progeroid Features. *The Journal of Clinical Endocrinology & Metabolism* **91**, 517–521, doi:10.1210/jc.2005-1297 (2006).
 36. Kosho, T. *et al.* Mandibuloacral dysplasia and a novel LMNA mutation in a woman with severe progressive skeletal changes. *Am J Med Genet A* **143A**, 2598–2603, doi:10.1002/ajmg.a.31983 (2007).
 37. Plasilova, M. *et al.* Discordant Gene Expression Signatures and Related Phenotypic Differences in Lamin A- and A/C-Related Hutchinson-Gilford Progeria Syndrome (HGPS). *PLoS ONE* **6**, e21433, doi:10.1371/journal.pone.0021433 (2011).
 38. Al-Haggar, M. *et al.* A novel homozygous p.Arg527Leu LMNA mutation in two unrelated Egyptian families causes overlapping mandibuloacral dysplasia and progeria syndrome. *European Journal of Human Genetics* **20**, 1134–1140, doi:10.1038/ejhg.2012.77 (2012).
 39. Starke, S. *et al.* Progeroid laminopathy with restrictive dermopathy-like features caused by an isodisomic LMNA mutation p.R435C. *Aging* **5**, 445–459, doi:10.18632/aging.100566 (2013).
 40. Bai, S. *et al.* Mandibuloacral Dysplasia Caused by LMNA Mutations and Uniparental Disomy. *Case Rep Genet* 2014, 508231, doi:10.1155/2014/508231 (2014).
 41. Sewairi, W., Assiri, A., Patel, N., Alhashem, A. & Alkuraya, F. S. Distal acroosteolysis, poikiloderma and joint stiffness: a novel laminopathy? *European Journal of Human Genetics* **24**, 1220–1222, doi:10.1038/ejhg.2015.265 (2016).

42. Yassaee, V. R., Khojaste, A., Hashemi-Gorji, F., Ravesh, Z. & Toosi, P. A novel homozygous LMNA mutation (p.Met540Ile) causes mandibuloacral dysplasia type A. *Gene* **577**, 8–13, doi:10.1016/j.gene.2015.08.071 (2016).
43. Zhang, S., Zhang, K., Jiang, M. & Zhao, J. Hutchinson-Gilford progeria syndrome with scleroderma-like skin changes due to a homozygous missense LMNA mutation. *Journal of the European Academy of Dermatology and Venereology* **30**, 463–465, doi:10.1111/jdv.12840 (2016).
44. Madej-Pilarczyk, A. *et al.* Progeroid syndrome with scleroderma-like skin changes associated with homozygous R435C LMNA mutation. *Am J Med Genet A* **149A**, 2387–2392, doi:10.1002/ajmg.a.33018 (2009).
45. Scharner, J., Lu, H. C., Fraternali, F., Ellis, J. A. & Zammit, P. S. Mapping disease-related missense mutations in the immunoglobulin-like fold domain of lamin A/C reveals novel genotype-phenotype associations for laminopathies. *Proteins* **82**, 904–915, doi:10.1002/prot.24465 (2014).
46. Barroso-Vilares, M. & Logarinho, E. Chromosomal instability and pro-inflammatory response in aging. *Mech Ageing Dev* **182**, 111118, doi:10.1016/j.mad.2019.111118 (2019).
47. Mu, X. *et al.* Cytoskeleton stiffness regulates cellular senescence and innate immune response in Hutchinson–Gilford Progeria Syndrome. *Aging Cell* **19**, doi:10.1111/accel.13152 (2020).
48. Yang, H., Wang, H., Ren, J., Chen, Q. & Chen, Z. J. cGAS is essential for cellular senescence. *Proceedings of the National Academy of Sciences* **114**, E4612–E4620, doi:10.1073/pnas.1705499114 (2017).
49. Sun, L., Wu, J., Du, F., Chen, X. & Chen, Z. J. Cyclic GMP-AMP synthase is a cytosolic DNA sensor that activates the type I interferon pathway. *Science* **339**, 786–791, doi:10.1126/science.1232458 (2013).
50. Hu, B. *et al.* The DNA-sensing AIM2 inflammasome controls radiation-induced cell death and tissue injury. *Science* **354**, 765–768, doi:10.1126/science.aaf7532 (2016).
51. Hornung, V. *et al.* AIM2 recognizes cytosolic dsDNA and forms a caspase-1-activating inflammasome with ASC. *Nature* **458**, 514–518, doi:10.1038/nature07725 (2009).
52. *Clinical Interventions in Aging* **Volume 3**, 431–444, doi:10.2147/cia.s1957 (2008).
53. Hutchison, C. J. & Worman, H. J. A-type lamins: guardians of the soma? *Nat Cell Biol* **6**, 1062–1067, doi:10.1038/ncb1104-1062 (2004).
54. Kennedy, B. K. & Pennypacker, J. K. 127–142 (Springer New York, 2014).
55. Vidak, S., Kubben, N., Dechat, T. & Foisner, R. Proliferation of progeria cells is enhanced by lamina-associated polypeptide 2 α (LAP2 α) through expression of extracellular matrix proteins. *Genes & Development* **29**, 2022–2036, doi:10.1101/gad.263939.115 (2015).
56. Musich, P. R. & Zou, Y. DNA-damage accumulation and replicative arrest in Hutchinson–Gilford progeria syndrome. *Biochemical Society Transactions* **39**, 1764–1769, doi:10.1042/bst20110687 (2011).
57. Gonzalez-Suarez, I. & Gonzalo, S. Nurturing the genome: A-type lamins preserve genomic stability. *Nucleus* **1**, 129–135, doi:10.4161/nucl.1.2.10797 (2010).

58. Ferreli, C. *et al.* Cutaneous Manifestations of Scleroderma and Scleroderma-Like Disorders: a Comprehensive Review. *Clinical Reviews in Allergy & Immunology* **53**, 306–336, doi:10.1007/s12016-017-8625-4 (2017).
59. Canalis, E. & Zanotti, S. Hajdu-Cheney syndrome: a review. *Orphanet J Rare Dis* **9**, 200, doi:10.1186/s13023-014-0200-y (2014).
60. Samson, C. *et al.* Structural analysis of the ternary complex between lamin A/C, BAF and emerin identifies an interface disrupted in autosomal recessive progeroid diseases. *Nucleic Acids Research* **46**, 10460–10473, doi:10.1093/nar/gky736 (2018).
61. Jamin, A. & Wiebe, M. S. Barrier to Autointegration Factor (BANF1): interwoven roles in nuclear structure, genome integrity, innate immunity, stress responses and progeria. *Curr Opin Cell Biol* **34**, 61–68, doi:10.1016/j.ceb.2015.05.006 (2015).
62. Dittmer, T. A. & Misteli, T. The lamin protein family. *Genome Biology* **12**, 222, doi:10.1186/gb-2011-12-5-222 (2011).
63. Cheedipudi, S. M. *et al.* Genomic Reorganization of Lamin-Associated Domains in Cardiac Myocytes Is Associated With Differential Gene Expression and DNA Methylation in Human Dilated Cardiomyopathy. *Circ Res* **124**, 1198–1213, doi:10.1161/CIRCRESAHA.118.314177 (2019).
64. Guey, B. *et al.* BAF restricts cGAS on nuclear DNA to prevent innate immune activation. *Science* **369**, 823–828, doi:10.1126/science.aaw6421 (2020).
65. Wagner, W. *et al.* Replicative senescence of mesenchymal stem cells: a continuous and organized process. *PLoS One* **3**, e2213, doi:10.1371/journal.pone.0002213 (2008).
66. Pollex, R. L. & Hegele, R. A. Hutchinson-Gilford progeria syndrome. *Clin Genet* **66**, 375–381, doi:10.1111/j.1399-0004.2004.00315.x (2004).
67. He, W. *et al.* Ageing potentiates diet-induced glucose intolerance, beta-cell failure and tissue inflammation through TLR4. *Sci Rep* **8**, 2767, doi:10.1038/s41598-018-20909-w (2018).
68. Spencer, S. J. *et al.* High-fat diet and aging interact to produce neuroinflammation and impair hippocampal- and amygdalar-dependent memory. *Neurobiol Aging* **58**, 88–101, doi:10.1016/j.neurobiolaging.2017.06.014 (2017).
69. Schreiber, K. H. & Kennedy, B. K. When lamins go bad: nuclear structure and disease. *Cell* **152**, 1365–1375, doi:10.1016/j.cell.2013.02.015 (2013).
70. Coll-Bonfill, N., Cancado de Faria, R., Bhoopatiraju, S. & Gonzalo, S. Calcitriol Prevents RAD51 Loss and cGAS-STING-IFN Response Triggered by Progerin. *Proteomics* **20**, e1800406, doi:10.1002/pmic.201800406 (2020).
71. Gonzalo, S. DNA damage and lamins. *Adv Exp Med Biol* **773**, 377–399, doi:10.1007/978-1-4899-8032-8_17 (2014).
72. Marcelot, A. *et al.* Di-phosphorylated BAF shows altered structural dynamics and binding to DNA, but interacts with its nuclear envelope partners. *Nucleic Acids Res* **49**, 3841–3855, doi:10.1093/nar/gkab184 (2021).

73. Franceschi, C. *et al.* Inflamm-aging. An evolutionary perspective on immunosenescence. *Ann N Y Acad Sci* **908**, 244–254, doi:10.1111/j.1749-6632.2000.tb06651.x (2000).
74. Köhler, F. *et al.* Epigenetic deregulation of lamina-associated domains in Hutchinson-Gilford progeria syndrome. *Genome Medicine* **12**, doi:10.1186/s13073-020-00749-y (2020).
75. Cao, L. *et al.* The Nuclear Matrix Protein SAFA Surveils Viral RNA and Facilitates Immunity by Activating Antiviral Enhancers and Super-enhancers. *Cell Host Microbe* **26**, 369–384 e368, doi:10.1016/j.chom.2019.08.010 (2019).
76. Paijo, J., Kaefer, V. & Kalinke, U. cGAMP Quantification in Virus-Infected Human Monocyte-Derived Cells by HPLC-Coupled Tandem Mass Spectrometry. *Methods Mol Biol* **1656**, 153–166, doi:10.1007/978-1-4939-7237-1_9 (2017).
77. Liao, Y., Smyth, G. K. & Shi, W. The R package Rsubread is easier, faster, cheaper and better for alignment and quantification of RNA sequencing reads. *Nucleic Acids Res* **47**, e47, doi:10.1093/nar/gkz114 (2019).
78. Feng, J. *et al.* GFOLD: a generalized fold change for ranking differentially expressed genes from RNA-seq data. *Bioinformatics* **28**, 2782–2788, doi:10.1093/bioinformatics/bts515 (2012).
79. Langmead, B. & Salzberg, S. L. Fast gapped-read alignment with Bowtie 2. *Nat Methods* **9**, 357–359, doi:10.1038/nmeth.1923 (2012).
80. Zhang, Y. *et al.* Model-based analysis of ChIP-Seq (MACS). *Genome Biol* **9**, R137, doi:10.1186/gb-2008-9-9-r137 (2008).
81. Quinlan, A. R. & Hall, I. M. BEDTools: a flexible suite of utilities for comparing genomic features. *Bioinformatics* **26**, 841–842, doi:10.1093/bioinformatics/btq033 (2010).

Figures



F1

Figure 1

LMNA mutant R527C results in an atypical Hutchinson-Gilford progeria syndrome with aberrant inflammation

a) DNA sequencing for exon 9 of LMNA in atypical progeria patient (Patient 1; P1) and carrier (II15). Arrows indicated the identified mutation, a C→T change at codon 527, which resulted in the replacement

of Arg (CGT) to Cys (TGT).

b) Pedigree for one of the three atypical progeria families. Carriers were shown as a half-filled symbol, patients were shown as filled black symbol. Males were represented as squares, females as circles.

c) qRT-PCR analysis of the telomere length of Patient 2 and Patient 3 (P2, P3) and their siblings (III2, III5, III6, III7, III8, III9, III15, III16) in the three atypical progeria families. $n = 3$.

d) Clinical signs of the patients with LMNA G608G heterozygous mutation (top) and R527C homozygous mutation (bottom; P1). Patients with R527C homozygous mutation showed severe scleroderma, acroosteolysis and arthritis.

e) Immunohistochemical analysis of the nuclear morphology and LMNA expression in the subcutaneous tissue of Healthy Donor 1 (left; HD1), patients with LMNA G608G heterozygous mutation (middle) and R527C homozygous mutation (right; P1). Scale Bar, 50 μ M. $n = 3$.

f) A flow chart depicting the process of sample preparing before RNA-seq analysis. PBMCs from patients and healthy donors were reprogrammed into iPSCs and were further differentiated into MSCs. RNA-seq analysis of the transcriptomes of PBMCs and MSCs.

g) GO analysis of the down-regulated genes in patient-derived PBMCs compared with healthy donor-derived PBMCs (*Fold Change (FC) < 0.25, P value < 0.05*).

h) GO analysis of the up-regulated genes in patient-derived PBMCs compared with healthy donor-derived PBMCs (*Fold Change (FC) > 4, P value < 0.05*).

i) Analysis of PRRs expression level which were increased in patient-derived PBMCs compared with healthy donor-derived PBMCs in RNA-seq data.

j) Analysis of ISGs expression level which were increased in patient-derived PBMCs compared with healthy donor-derived PBMCs in RNA-seq data.

k) GO analysis of the down-regulated genes in patient-derived $LMNA^{R527C/R527C}$ MSCs compared with control (top) and $LMNA^{WT/G608G}$ MSCs compared with control (bottom) (*Fold Change (FC) < 0.25, P value < 0.05*).

l) GO analysis of the up-regulated genes in patient-derived $LMNA^{R527C/R527C}$ MSCs compared with control (top) and $LMNA^{WT/G608G}$ MSCs compared with control (bottom) (*Fold Change (FC) > 4, P value < 0.05*). (* $P < 0.05$)

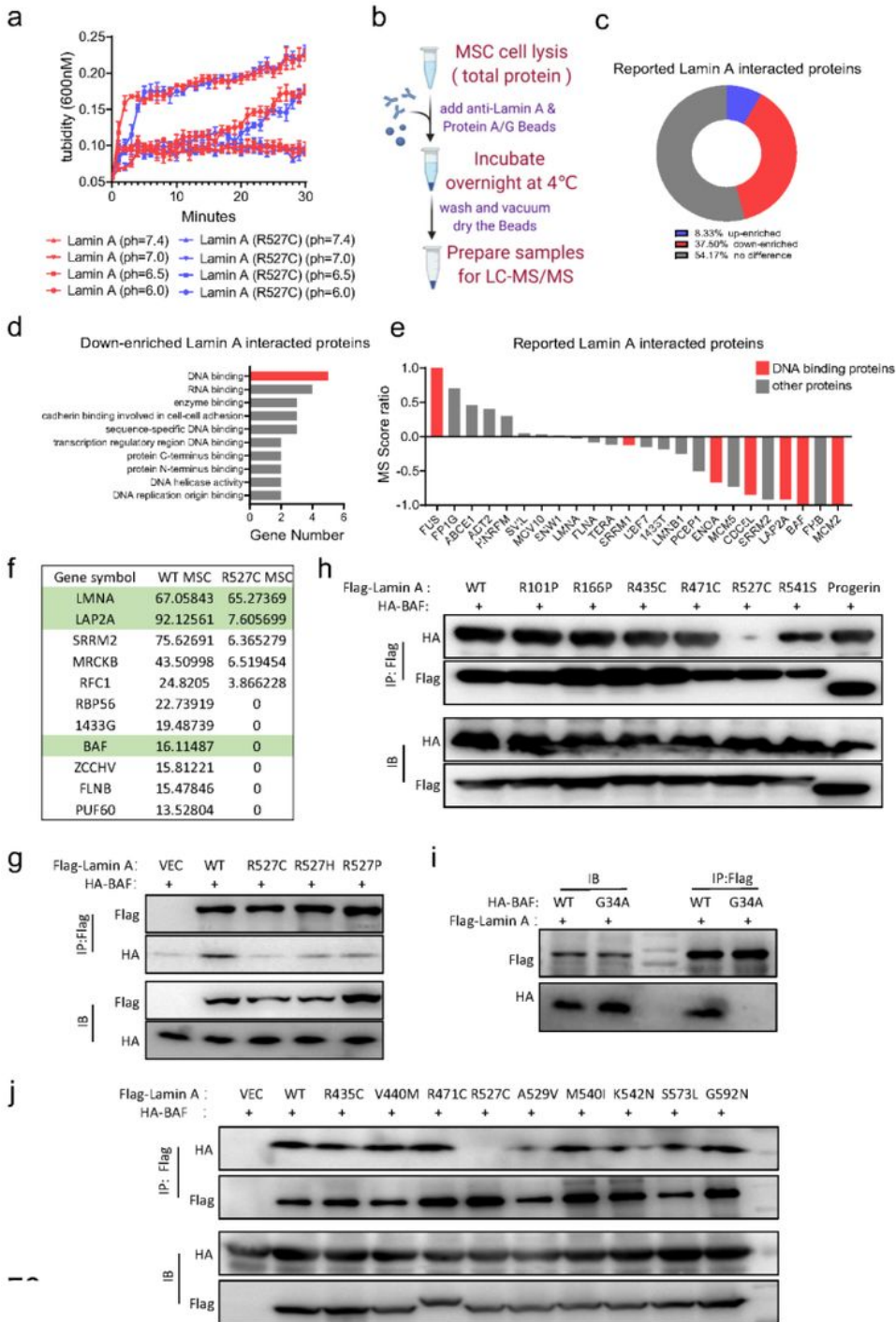
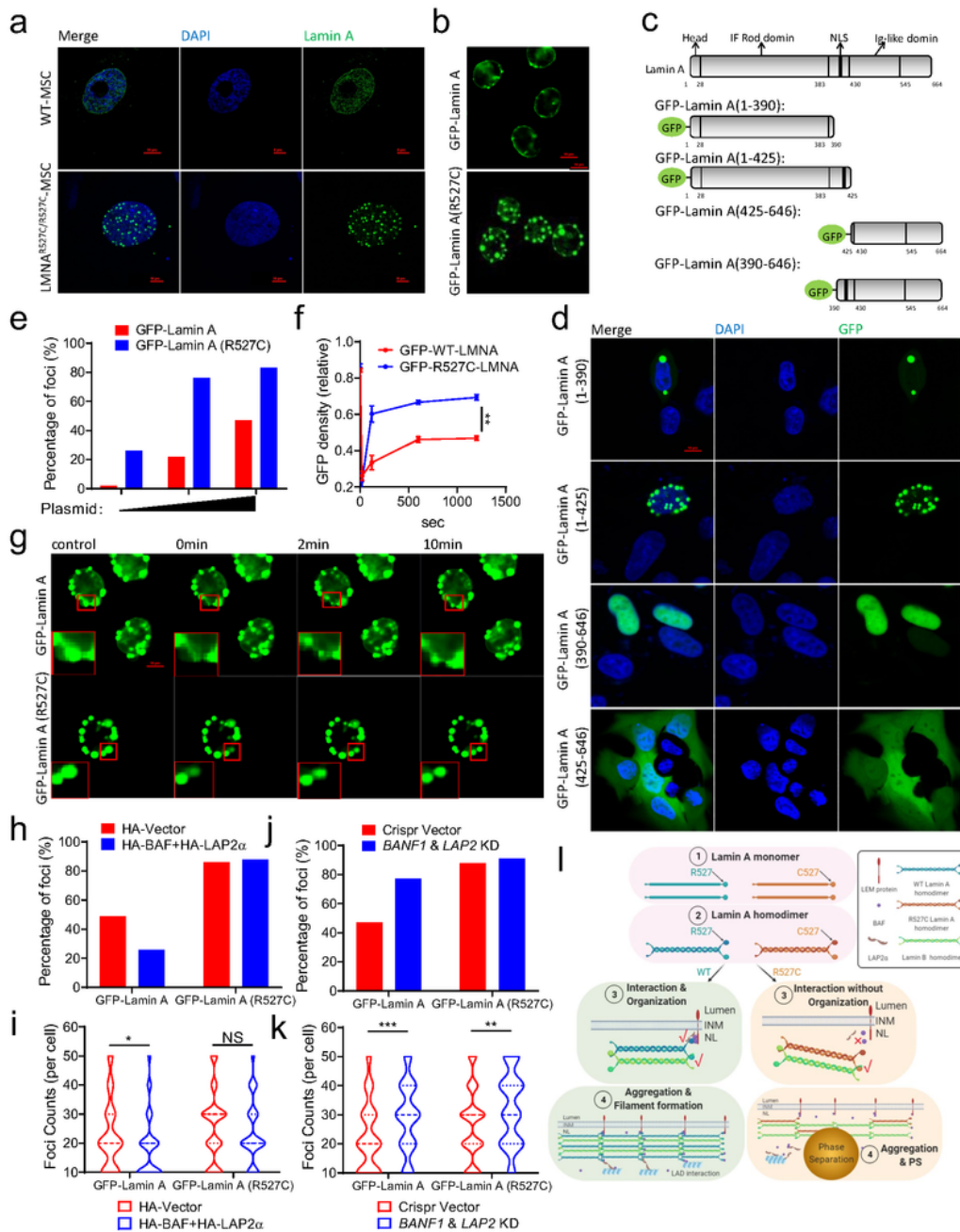


Figure 2

LMNA R527C mutation dampens its interaction with DNA binding proteins

a) Turbidity assay analysis of the droplet and filament formation of wild type and R527C mutant Lamin A proteins during different PH at 10 μ M. $n = 3$.

- b) A flow chart depicting the process of immunoprecipitation experiments to detect proteins interacted with wild type and R527C mutant Lamin A. Endogenous Lamin A and Lamin A interacted proteins were enriched by Lamin A antibody from MSCs lysis. Mass spectrum analysis of protein enrichment of Lamin A interacted protein.
- c) Analysis of the enrichment difference of reported Lamin A interacted proteins between wild type and R527C mutant Lamin A in mass spectrum results.
- d) GO analysis of the down-enriched proteins immunoprecipitated by R527C mutant Lamin A compared with wild type Lamin A.
- e) Quantification of the reported Lamin A interacted proteins in mass spectrum results. Ordinate showed the rate of MS score between wild type and R527C mutant Lamin A (0 means protein was immunoprecipitated equally by wild type and R527C mutant Lamin A, 1 means the protein was only enriched in R527C mutant Lamin A, -1 means the protein was only enriched in wild type Lamin A).
- f) MS score of the selected proteins in mass spectrum results.
- g) Co-immunoprecipitation analysis of the interaction between exogenous HA-BAF and wild type, R527C, R527H, R527P mutant Flag-Lamin A. $n = 3$.
- h) Co-immunoprecipitation assay analysis of the interaction between exogenous Flag-Lamin A and wild type, NGPS mutant HA-BAF. $n = 3$.
- i) Co-immunoprecipitation assay analysis of the interaction between exogenous HA-BAF and different pathogenic arginine mutant Flag-Lamin A or Flag-progerin. $n = 3$.
- j) Co-immunoprecipitation assay analysis of the interaction between exogenous HA-BAF and different homozygous pathogenic mutant Flag-Lamin A. $n = 3$. (*NS = No significant; *P < 0.05; **P < 0.01*)



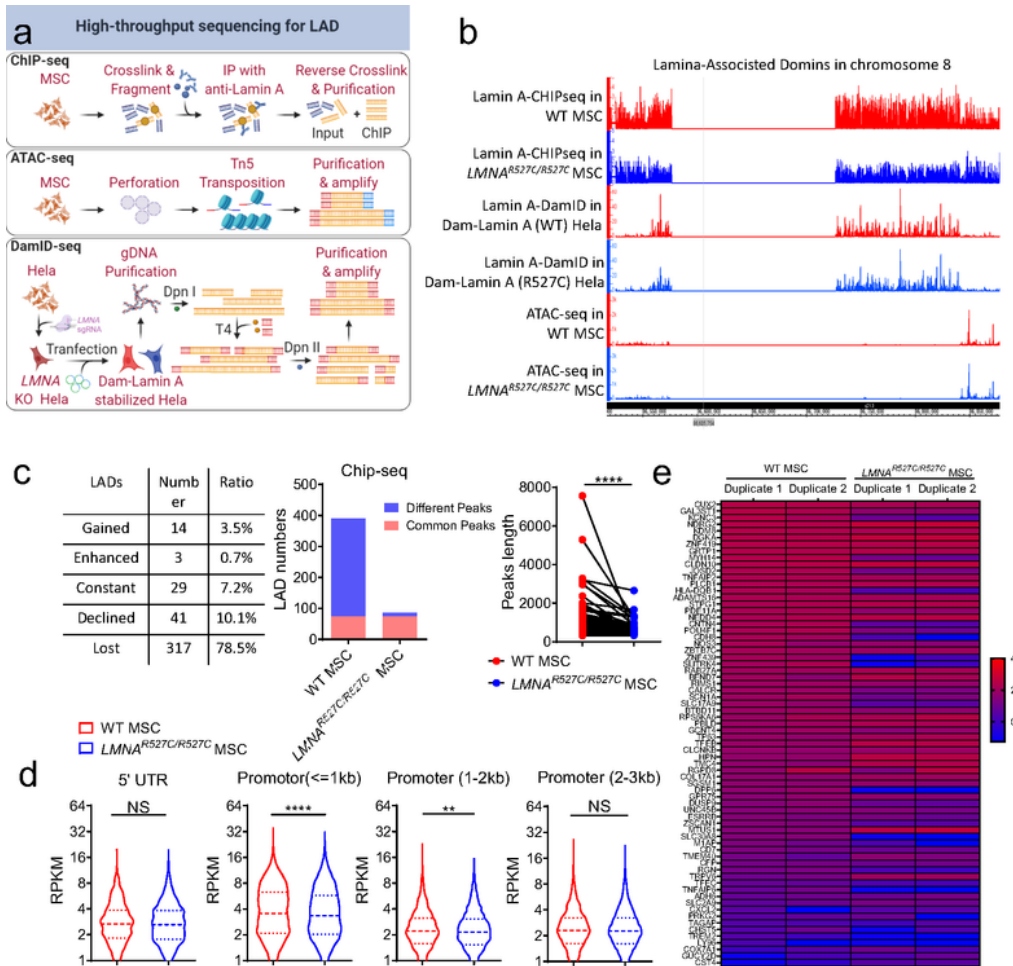
F3

Figure 3

R527C mutation promotes self-aggregation of Lamin A

a) Laser scanning confocal microscope (LSCM) analysis of endogenous Lamin A (green) localization and morphology in patient-derived MSCs and control MSCs. R527C mutant Lamin A had foci formation in patient-derived MSCs (1%). Scale Bar, 10 μ M. $n = 3$.

- b) LSCM analysis of the localization and morphology of wild type and R527C mutant GFP-Lamin A. Wild type and R527C mutant GFP-Lamin A were overexpressed in *LMNA*^{-/-} HeLa cells. Scale Bar, 10 μ M. *n* = 3.
- c) A flow chart depicting different GFP-Lamin A truncation constructs to investigate the characteristic of Lamin A foci formation. Different GFP-Lamin A truncations were overexpressed in *LMNA*^{-/-} HeLa cells. LSCM analysis of the foci formation and dynamic of different GFP-Lamin A truncations.
- d) LSCM analysis of the localization and morphology of different GFP-Lamin A truncations. Different GFP-Lamin A truncations were overexpressed in *LMNA*^{-/-} HeLa cells. Scale Bar, 10 μ M. *n* = 3.
- e) Quantification of GFP-Lamin A foci forming cell ratio. Different amounts of wild type and R527C mutant GFP-Lamin A plasmids were transfected into *LMNA*^{-/-} HeLa cells. GFP-Lamin A foci were observed by LSCM.
- f) FRAP curve analysis of the dynamic ability of wild type and R527C mutant GFP-Lamin A. wild type and R527C mutant GFP-Lamin A were stabilized in *LMNA*^{-/-} HeLa cells. *n* = 3.
- g) Fluorescence recovery after photobleaching (FRAP) analysis of the dynamic ability of wild type and R527C mutant GFP-Lamin A. wild type and R527C mutant GFP-Lamin A were stabilized in *LMNA*^{-/-} HeLa cells. Scale Bar, 10 μ M. *n* = 3.
- h) Quantification of GFP-Lamin A foci forming cell ratio. Wild type and R527C mutant GFP-Lamin A were stabilized in *LMNA*^{-/-} HeLa cells, with or without exogenous HA-LAP2 α and HA-BAF overexpression. GFP-Lamin A foci were observed by LSCM.
- i) Quantification of GFP-Lamin A foci number in cells. Wild type and R527C mutant GFP-Lamin A were stabilized in *LMNA*^{-/-} HeLa cells, with or without exogenous HA-LAP2 α and HA-BAF overexpression. GFP-Lamin A foci were observed by LSCM.
- j) Quantification of GFP-Lamin A foci forming cell ratio. Wild type and R527C mutant GFP-Lamin A were stabilized in *LMNA*^{-/-} HeLa cells, with or without *LAP2* and *BANF1* knocked down. GFP-Lamin A foci were observed by LSCM.
- k) Quantification of GFP-Lamin A foci number in cells. Wild type and R527C mutant GFP-Lamin A were stabilized in *LMNA*^{-/-} HeLa cells, with or without *LAP2* and *BANF1* knocked down. GFP-Lamin A foci were observed by LSCM. (***P* < 0.01; ****P* < 0.001)
- l) A flow chart depicting the principle of R527C mutant Lamin A foci formation under physiological conditions. R527C mutant Lamin A tended to aggregated and form foci spontaneously due to damp the interaction with BAF and LAP2 α . (*NS* = No significant; ***P* < 0.01; ****P* < 0.001; *****P* < 0.0001)



F4

Figure 4

R527C mutation damps the interactions between LMNA and LADs

a) A flow chart depicting the high-throughput sequencing experiments process for detecting the Lamin A-LADs binding affinity of wild type and R527C mutant Lamin A. Lamin A Chip-seq and ATAC-seq were performed in patient-derived MSCs and control MSCs. DamID-seq were performed in *LMNA*^{-/-} HeLa cells.

- b) A genome browser map depicting LADs and Lamin A-LADs binding affinity of chromosome 8 in wild type and R527C Lamin A mutant cells. Ordinate of Lamin A Chip-seq were Chip/input signal ratio, ordinate of Lamin A DamID-seq were Dam-LMNA/Dam signal ratio and ordinate of ATAC-seq were RPKM level. Control cells were showed as red peaks and Lamin A R527C mutant cells were showed as blue peaks.
- c) Graphs quantification of the Lamin A-LADs binding affinity between wild type and R527C mutant Lamin A in Chip-seq. Table depicting the Chip/input signal ratio change in patient-derived MSCs compared with control MSCs during whole genome (left). Panel depicting the total LADs number identified in patient-derived MSCs and control MSCs (middle). Panel depicting the length of ChIP-seq peaks which were enriched in both patient-derived MSCs and control MSCs (right).
- d) Analysis of ATAC-seq RPKM level of different regions (5'UTR, Promoter \leq 1kb, Promoter 1-2kb, Promoter 2-3kb, from left to right) in patient-derived MSCs and control MSCs after parameter adjusted.
- e) Heat map depicting the selected genes expression in patient-derived MSCs compared with control MSCs. Genes were selected by ATAC-seq which promoter (\leq 1kb) regions were down-enrichment (*Fold Change (FC) < 0.1, P value < 0.05*). (*NS = No significant; **P < 0.01; ****P < 0.0001*)

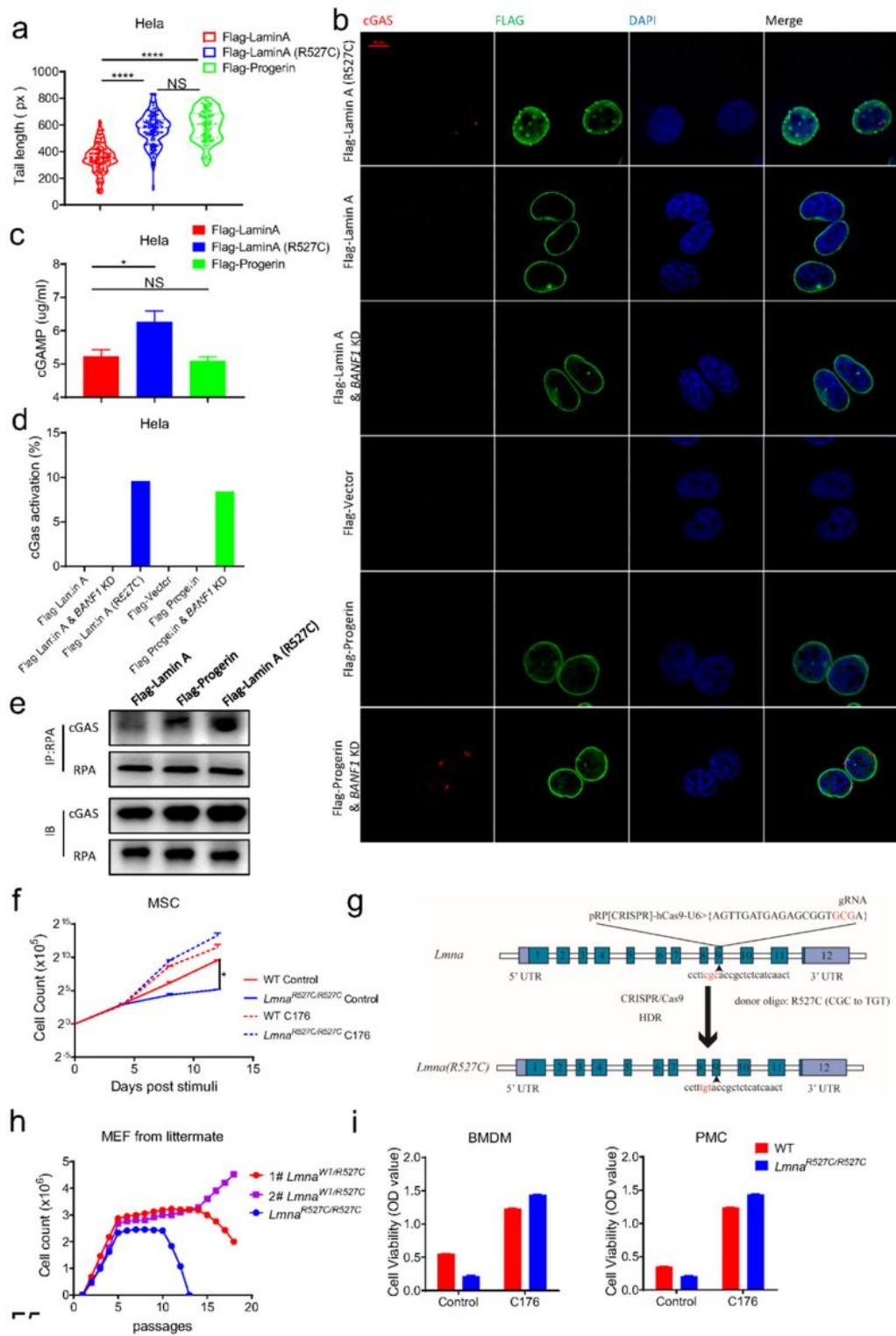
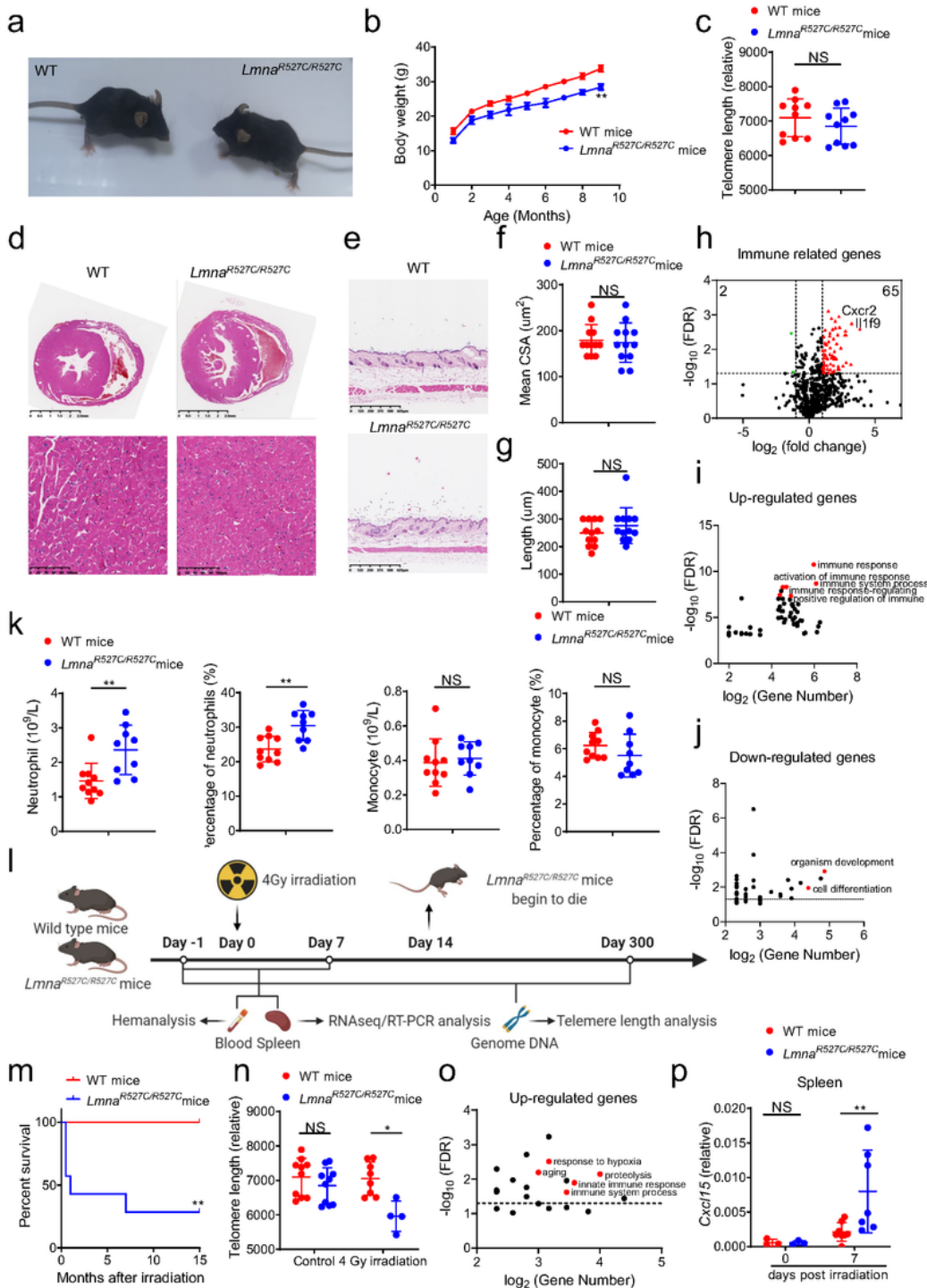


Figure 5

Hyperactivation of cGAS-STING pathway in R527C mutant cells

a) Comet tail assay analysis of DNA damage level of different Lamin A stabilized cells. Wild type or R527C mutant Flag-Lamin A were stabilized in *LMNA*^{-/-} HeLa cells and Flag-Progerin were stabilized in wild type HeLa cells.

- b) LSCM analysis of endogenous cGAS (red) activation and exogenous Flag-Lamin A (green) morphology with or without *BANF1* knockdown. Wild type or R527C mutant Flag-Lamin A were stabilized in *LMNA*^{-/-} Hela cells, Flag-Vector or Flag-Progerin were stabilized in wild type Hela cells. Scale Bar, 10μM. *n* = 3.
- c) Mass spectrum analysis of cGAMP concentrations in different Lamin A stabilized cells. Wild type or R527C mutant Flag-Lamin A were stabilized in *LMNA*^{-/-} Hela cells and Flag-Progerin were stabilized in wild type Hela cells. *n* = 3.
- d) Quantification of cGAS activating cell ratio. Wild type or R527C mutant Flag-Lamin A were stabilized in *LMNA*^{-/-} Hela cells, Flag-Vector or Flag-Progerin were stabilized in wild type Hela cells. cGAS activating were observed by LSCM.
- e) Western blot analysis of cGAS protein enrichment in different Lamin A stabilized cells during RPA ChIP. Wild type or R527C mutant Flag-Lamin A were stabilized in *LMNA*^{-/-} Hela cells and Flag-Progerin were stabilized in wild type Hela cells. *n* = 3. *n* = 3.
- f) Cell viability assay analysis of the proliferation rates of patient-derived MSCs and control MSCs. Patient-derived MSCs and control MSCs were treated with or without C176 (1nM). *n* = 3.
- g) A flow chart depicting the principle of *Lmna*^{R527C/R527C} mice model editing. CRISPR/Cas9 system was used to mutate LMNA gene in mice.
- h) Growth curve of MEFs derived from littermate *Lmna*^{WT/R527C} and *Lmna*^{R527C/R527C} embryos according to a MEF immortalization protocol⁴⁸. Briefly, MEFs were counted and cultured until 20st passage.
- i) Cell viability assay analysis of the senescence level of wild type and R527C mutant murine cells. Bone marrow macrophages (left) and peritoneal macrophages (right) were treated with or without C176 (10nM). Cell viability were examined at 28 days post cell cultivation. *n* = 3. (NS = No significant; **P* < 0.05; *****P* < 0.0001)



F6

Figure 6

Lmna^{R527C/R527C} mice exhibit elevated inflammation but no typical progeria symptoms

a) Picture depicting body shape of wild type and *Lmna*^{R527C/R527C} mice at 6 weeks old.

b) Analysis of body weight change of wild type and *Lmna*^{R527C/R527C} mice. *n* = 10.

- c) qRT-PCR analysis of telomere length of wild type and *Lmna*^{R527C/R527C} mice at 7 months old. *n* = 10.
- d) H&E histochemical analysis of cross section through the heart tissue of wild type and *Lmna*^{R527C/R527C} mice at 8 months old. *n* = 3.
- e) H&E histochemical analysis of subcutaneous tissue of wild type and *Lmna*^{R527C/R527C} mice at 8 months old. *n* = 3.
- f) Quantification of cardiomyocyte mean cross-section area (CSA) of wild type and *Lmna*^{R527C/R527C} mice at 8 months old. *n* = 3.
- g) Quantification of subcutaneous adipose tissue thickness of wild type and *Lmna*^{R527C/R527C} mice at 8 months old. *n* = 3.
- h) Volcano plots depicting the immune-related genes expression in the spleen of *Lmna*^{R527C/R527C} mice compared with wild type mice at 6 weeks old.
- i) GO analysis of the up-regulated genes in the spleen of *Lmna*^{R527C/R527C} mice compared with wild type mice (*Fold Change (FC)* > 4, *P value* < 0.05).
- j) GO analysis of the down-regulated genes in the spleen of *Lmna*^{R527C/R527C} mice compared with wild type mice (*Fold Change (FC)* < 0.25, *P value* < 0.05).
- k) Hemanalysis of counts and ratios of neutrophil (left) and monocyte (right) in wild type and *Lmna*^{R527C/R527C} mice at 6 weeks old. *n* = 9-10.
- l) A flow chart depicting the process of mice irradiation experiments. Wild type and *Lmna*^{R527C/R527C} mice were treated with 4 Gy irradiation at 6 weeks old. Blood and spleen were collected at 0 and 7 days post irradiation (dpi) for hemanalysis, qRT-PCR and RNA-seq. Genome DNA were collected at 0 dpi and 300 dpi for telomere length analysis. Survival curve and body weight change were monitored daily.
- m) Analysis of survival curve of wild type and *Lmna*^{R527C/R527C} mice treated with 4 Gy irradiation. *n* = 7.
- n) qRT-PCR analysis of telomere length of wild type and *Lmna*^{R527C/R527C} mice treated with 4 Gy irradiation at 0 dpi and 300 dpi. *n* = 2-5.
- o) GO analysis of the up-regulated genes in the spleen of *Lmna*^{R527C/R527C} mice compared with wild type mice treated with 4 Gy irradiation at 7 dpi (*Fold Change (FC)* > 4, *P value* < 0.05).
- p) qRT-PCR analysis of *Cxcl15* expression in the spleen of wild type and *Lmna*^{R527C/R527C} mice treated with 4 Gy irradiation at 0 dpi and 7 dpi. *n* = 3-7. (*NS* = No significant; **P* < 0.05; ***P* < 0.01)

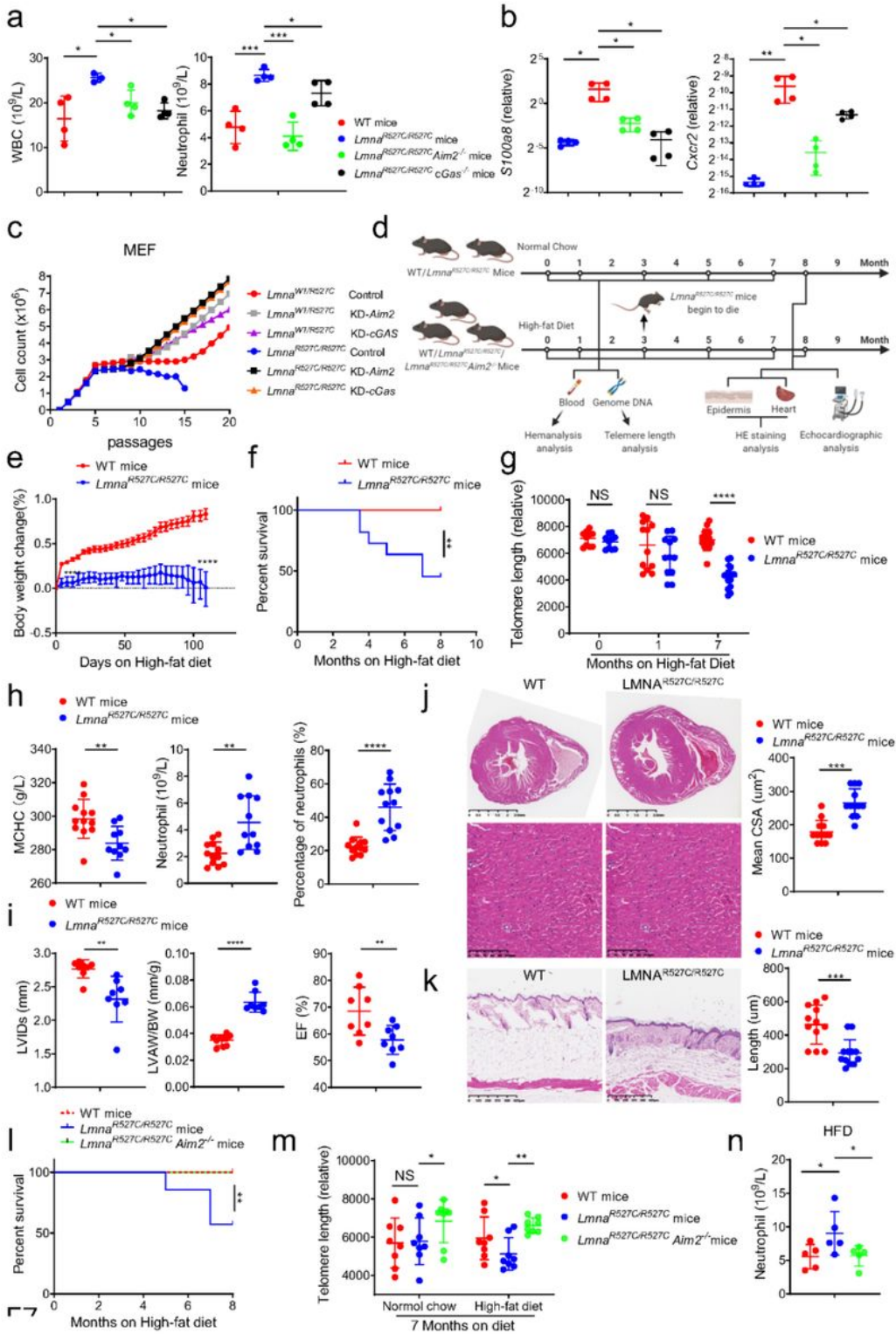


Figure 7

HFD causes premature aging of *Lmna*^{R527C/R527C} mice in a DNA sensing pathway dependent manner

a) Hemanalysis of white blood cell counts (left) and neutrophil counts (right) of wild type, *Lmna*^{R527C/R527C}, *Lmna*^{R527C/R527C}*Aim2*^{-/-} and *Lmna*^{R527C/R527C}*cGas*^{-/-} mice at 6 weeks old. *n* = 4.

- b) qRT-PCR analysis of *S100a8* and *Cxcr2* expression in the spleen of wild type, *Lmna*^{R527C/R527C}, *Lmna*^{R527C/R527C}*Aim2*^{-/-} and *Lmna*^{R527C/R527C}*cGas*^{-/-} mice at 6 weeks old. *n* = 4.
- c) Growth curve of MEFs derived from littermate *Lmna*^{WT/R527C} and *Lmna*^{R527C/R527C} embryos according to a MEF immortalization protocol. Briefly, MEFs were treated with or without *Cgas/Aim2* knock down and were counted and cultured until 20st passage.
- d) A flow chart depicting the process of mice high-fat diet experiments. Wild type, *Lmna*^{R527C/R527C} and *LMNA*^{R527C/R527C}*Aim2*^{-/-} mice were fed with high-fat diet after 6 weeks old. Blood and genome DNA were collected at 0, 1, 3, 5 and 7 months after high-fat diet for hemanalysis and telomere length analysis. H&E histochemical analysis and echocardiographic analysis were performed at 8 months after high-fat diet.
- e) Analysis of body weight change of wild type and *Lmna*^{R527C/R527C} mice after high-fat diet. *n* = 13.
- f) Analysis of survival curve of wild type and *Lmna*^{R527C/R527C} mice on high-fat diet. *n* = 13.
- g) qRT-PCR analysis of telomere length of wild type and *Lmna*^{R527C/R527C} mice at 0, 1 and 7 months after high-fat diet. *n* = 13.
- h) Hemanalysis of mean corpuscular hemoglobin (MCH; left) and neutrophil (right) of wild type and *lmna*^{R527C/R527C} mice at 1 month after high-fat diet. *n* = 12
- i) Echocardiographic analysis of left ventricular internal diameter at end-systole (LVIDs; left), anterior left ventricular wall (LVAW; middle) and ejection fraction (EF; right) of wild type and *Lmna*^{R527C/R527C} mice at 8 months after high-fat diet. *n* = 3-5.
- j) H&E histochemical analysis of cross section through the heart tissue of wild type and *Lmna*^{R527C/R527C} mice at 8 months after high-fat diet (left). Quantification of cardiomyocyte mean cross-section area (CSA) of wild type and *Lmna*^{R527C/R527C} mice at 8 months after high-fat diet (right). *n* = 5.
- k) H&E histochemical analysis of subcutaneous tissue of wild type and *Lmna*^{R527C/R527C} mice at 8 months after high-fat diet (left). Quantification of subcutaneous adipose tissue thickness of wild type and *Lmna*^{R527C/R527C} mice at 8 months after high-fat diet (right). *n* = 3.
- l) Analysis of survival curve of wild type, *Lmna*^{R527C/R527C} and *Lmna*^{R527C/R527C}*Aim2*^{-/-} mice after high-fat diet. *n* = 7.
- m) qRT-PCR analysis of telomere length of wild type, *Lmna*^{R527C/R527C} and *Lmna*^{R527C/R527C}*Aim2*^{-/-} mice at 7 months after normal chow or high-fat diet. *n* = 4
- n) Hemanalysis of neutrophil counts of wild type, *Lmna*^{R527C/R527C} and *Lmna*^{R527C/R527C}*Aim2*^{-/-} mice at 1 months after high-fat diet. *n* = 5. (*NS* = No significant; **P* < 0.05; ***P* < 0.01; ****P* < 0.001; *****P* < 0.0001)

Supplementary Files

This is a list of supplementary files associated with this preprint. Click to download.

- [TableS1.xlsx](#)
- [TableS2.xlsx](#)
- [TableS3.xlsx](#)
- [ExtendedData.docx](#)